Emission Mössbauer spectroscopy study of undoped and Ba-doped $BiFeO_3$ thin films

by

Kimara Naicker

Submitted in fulfilment of the academic requirements for the degree of Master of Science in the School of Chemistry and Physics, University of KwaZulu-Natal, Westville campus

May 2019

CERN-THESIS-2019-325
24/04/2019

As the candidate's supervisor, I have approved this dissertation for submission.

Signed: _____ Name: Prof. K. Bharuth-Ram Date: 29.04.2019

PREFACE

The experimental aspects of the work presented in this dissertation were performed at the radioactive ion beam facility ISOLDE (Isotope Separator On Line Device) at CERN, Geneva, as part of a project on “Emission Mössbauer Spectroscopy of advanced materials for opto- and nano- electronics”.

The measurements were carried out within the Mössbauer Collaboration (Experiment IS630) with the following participating organizations: University of Kwa-Zulu-Natal, Durban University of Technology, the University of the Witwatersrand, Technical University of Ilmenau, Johannes Gutenberg University of Mainz and University of Duisburg-Essen (Germany), Johannes Kepler University (Austria), the Laboratorio Nazionale MDM CNR-INFM (Italy), University of Iceland (Iceland) and University of the Bilbao (Spain).

Preparation and characterization of the monocrystalline BFO and Ba-doped BFO samples were carried out at the University of Duisburg-Essen by Dr Juliana Schell and her colleagues. I participated in all aspects of the beam time in September 2018, from the setting up of the implantation chamber, detector and data acquisition system, and in the data acquisition on a host of samples including the samples studied as part of my degree project.

The data analysis, interpretation of the results and their correlation with previous measurements were carried out in the School of Chemistry and Physics, University of KwaZulu-Natal, under the supervision of Professor Krishanlal Bharuth-Ram.

I declare that the results presented in this dissertation are the original work of the author and have not otherwise been submitted in any form for any degree or diploma to any tertiary institution. Where use has been made of the work of others it is duly acknowledged in the text.

DECLARATION - PLAGIARISM

I, Kimara Naicker, declare that

1. The research reported in this dissertation, except where otherwise indicated, is my original research.

2. This dissertation has not been submitted for any degree or examination at any other university.

3. This dissertation does not contain other persons' data, pictures, graphs or other information, unless specifically acknowledged as being sourced from other persons.

4. This dissertation does not contain other persons' writing, unless specifically acknowledged as being sourced from other researchers. Where other written sources have been quoted, then:

a. Their words have been rewritten but the general information attributed to them has been referenced

b. Where their exact words have been used, then their writing has been placed in italics and inside quotation marks and referenced.

5. This dissertation does not contain text, graphics or tables copied and pasted from the Internet, unless specifically acknowledged, and the source being detailed in the dissertation and in the References sections.

Signed: Date: 09 August 2019

Abstract

This dissertation presents the use of emission Mössbauer Spectroscopy (eMS), following the implantation of radioactive ^{57}Mn* which β-decays to the 14.4 keV Mössbauer state of ^{57}Fe, to study the magnetic behaviour of undoped and Ba-doped $BiFeO_3$ (BFO). The measurements were conducted within the Emission Mössbauer Collaboration at the on-line radioactive ion beam facility, ISOLDE, at CERN where the radioactive ions are produced by the fission of a UC_2 target induced by bombardment with 1.2 GeV protons. After multi-stage laser ionization and electrostatic mass separation, the extracted ^{57}Mn ions are accelerated to 45 keV energy and implanted into the samples under study.

Undoped and doped BFO samples with a Ba content of 15% were prepared by pulsed laser deposition from a target with 20% Bismuth excess. ^{57}Fe-eMS data of 94 and 300 nm thick BBFO films and an undoped BFO sample were collected as a function of temperature, using a parallel plate avalanche counter in which one stainless-steel electrode was enriched to 90% in ^{57}Fe. The counter was mounted outside the implantation chamber, at 90° to the Mn beam direction.

The eMS spectra were dominated by a broad central doublet together with sextet structure in the wings. Simultaneous analysis of the spectra with the software code VINDA allowed the sextets structure to be resolved into a sextet due to probe Fe ions located at the Fe sites in the BFO and BBFO lattice (Fe_{BFO}) and a broad magnetic distribution due to Fe at defect sites such as oxygen vacancies.

The main focus of the study was the temperature-dependent behaviour of the magnetic field at the Fe sites in the undoped and Ba-doped samples (Fe_{BFO}). The main component of the magnetic sextet was characterized by a hyperfine field with room temperature values B_{hf} = 46.2 (1) T in the undoped sample and B_{hf} = 42.9 (6) T in the two Ba-doped samples. The isomer shift for all three samples, δ = 0.36(1) mm/s, was characteristic of Fe^{3+} in the high spin 5/2 state. Two features characterised the temperature-dependence of B_{hf} : i) the magnitude of B_{hf} showed a strong decrease as the temperature was increased, and ii) the intensity (spectral area) decreased rapidly at higher temperatures. Result (ii) made it a lot more difficult

to extract the B_{hf} values at higher temperatures. However, the temperature dependence of the magnetic component of the Ba-doped $BiFeO_3$ follows that of a ferromagnetic material and confirms that the anti-ferromagnetic virgin BFO film underwent a phase transformation on doping with Ba ions.

Acknowledgements

I am greatly indebted to my supervisor, Prof Krishanlal Bharuth-Ram, for his mentorship and guidance during my studies and for bringing me into international collaborations. I appreciate his efforts and time taken to read through analysis reports and the drafts of my dissertation with a critical eye and for his encouragements, comments, suggestions, and time consuming consultations in spite of various other commitments.

I am greatly thankful to Dr Juliana Schell, the BMBF Coordinator of the Solid State Physics Program at ISOLDE/CERN, who introduced me to this project during my CERN Summer Scholar stay at CERN in July – August 2018 and for her advice during the experimental work at ISOLDE. Moreover, I would like to express my appreciation to Dr Hilary Masenda and the members of the $^{57}Mn^{*}$ Mössbauer Collaboration at ISOLDE who participated in the beam time in 2018 and from whom I learnt all about emission Mössbauer Spectroscopy and its applications. Furthermore, I am grateful to Marianela Escolar, Sven Becker and Gerhard Jakob for preparation of all samples.

I am grateful for funding from the National Research Foundation (NRF) through the block grant bursary scheme, the SA-CERN program for funding all ISOLDE related trips covering air fares, accommodation and subsistence.

Many thanks to both academic and administrative staff in the School of Chemistry and Physics, University of KwaZulu-Natal and at iThemba LABS, Cape Town, who have contributed in any way towards my studies.

I would like to thank God for giving me the strength, knowledge, ability and opportunity to undertake this research study and to persevere and complete it satisfactorily. I give sincere thanks to my parents, Inbanathan and Adhika Naicker, my partner, Sylvain Pillay and my family for their unwavering and unconditional love, support and encouragement in all of my pursuits.

Romans 8:31 - What shall we then say to these things? If God be for us, who can be against us?

Table of Contents

PREFACE ..... *ii*

Abstract ..... *v*

Acknowledgements ..... *vii*

Table of Contents ..... *viii*

List of Figures and Tables ..... *x*

1 INTRODUCTION *1*

1.1 Background of Bismuth Ferrite (BFO) and requirement for doping **1**

1.2 Literature review of Barium doped Bismuth Ferrite (BBFO) **5**

1.3 Aims and Objectives of the study **9**

2 THEORY *11*

2.1 The Mössbauer Effect **11**

2.2 Factors contributing towards the Mössbauer effect **11**

2.2.1 Nuclear resonance fluorescence 11

2.2.2 Recoil energy 13

2.2.3 Recoil-free fraction 14

2.2.4 Natural line width 16

2.2.5 Spectral line shape 16

2.3 Mössbauer spectra **17**

2.3.1 Relative intensities of resonance lines in Mössbauer spectra 18

2.4 Relaxation effects on Mössbauer spectra **21**

2.4.1 Paramagnetic relaxation 24

2.4.1.1 Electronic spin-lattice relaxation 24

2.4.1.2 Electronic spin-spin relaxation 25

2.5 Hyperfine interaction parameters **26**

2.5.1 Isomer shift 26

2.5.1.1 Second order Doppler shift 28

2.5.2 Quadrupole splitting 29

2.5.3 Magnetic dipole interaction 31
2.5.4 Combined magnetic and quadrupole interactions 33

3 EXPERIMENTAL DETAILS 35

3.1 Sample description and preparation 35

3.2 Emission Mössbauer spectroscopy at the ISOLDE facility 37

3.2.1 Beam production 39
3.2.2 Experimental set-up 43

3.3 eMS measurements 46

4 RESULTS AND DISCUSSION 48

4.1 Analysis of data and results of BBFO sample of thickness 94 nm 48

4.1.1 Mössbauer spectra 48
4.1.2 Hyperfine parameters 51
4.1.3 Annealing behavior 51

4.2 Analysis of data and results of BBFO sample of thickness 300 nm 53

4.2.1 Mössbauer spectra 53
4.2.2 Hyperfine parameters 55
4.2.3 Annealing behavior 55

4.3 Analysis of data and results of the undoped BFO sample 57

4.3.1 Mössbauer spectra 57
4.3.2 Hyperfine parameters 58
4.3.3 Annealing behavior 59

4.4 Temperature dependence of the magnetic field B_{hf} of the primary sextet 59

5 CONCLUSIONS 62

REFERENCES 64

List of Figures and Tables

Figure 1.1: The electric field, E, magnetic field, H and stress, σ control the electric polarization, P, magnetization, M, and strain, ε respectively. In a ferroic material, P, M or ε produce ferromagnetism, ferroelectricity or ferroelasticity, respectively. In a magnetoelectric multiferroic, a magnetic field may control P, or an electric field may control M, this is indicated as green arrows [1]. 2

Figure 1.2: Schematic view of the rhombohedrally distorted perovskite structure in the R3c space group representation of bismuth ferrite. The vectors denote the spins of Fe ions [10]. Here, in the ABO_3 phase, Bismuth is placed at the A-site and Iron at the B-site. 3

Figure 2.1: Non-resonant gamma-ray absorption as a result of loss in energy as recoil energy [24]. 12

Figure 2.2: Resonant emission and absorption of gamma rays between nucleii and resonance fluorescence and conversion electrons [24].....13

Figure 2.3: Effect of recoil on a nucleus of mass M and resulting energies [27].....13

Figure 2.4: Intensity distribution for gamma-ray emission dependent on transition energy $E0$ where e is the excited state and g is the ground state [24]. 17

Figure 2.5 : The development of an emission Mössbauer spectrum, as presented in ref. [24]. 18

Table 2.1: Classification of multipoles in electromagnetic transitions [27]. 19

Table 2.2(a): Relative probabilities for a dipole 3/2→ 1/2 transition. C^2 and $\boldsymbol{\Theta}$ are normalized angular independent and dependent terms. [25]. 20

Table 2.2(b) Clebsch-Gordan and angle-dependent coefficients for Electric Quadrupole 3/2 → ½ transitions. 21

Figure 2.6: Theoretical ^{57}Fe Mössbauer relaxation spectra for longitudinal relaxation [29]. 23

Figure 2.7: Scale of relaxation times [26]. 24

Figure 2.8: Processes that contribute to spin-lattice relaxation - (a) Direct process and (b) Raman process. 25

Figure 2.9: The isomer shifts and the resulting emission Mössbauer spectrum [28]. 28

Figure 2.10: The quadrupole splitting and the resulting emission Mössbauer spectrum [28]. 31

Figure 2.11.: The energy level shifts and the resulting Mössbauer spectra for magnetic dipole interaction in the absence and presence of an electric field gradient [28]. 33
Figure 3.1: Atomic force microscopy image of surface topography of a Ba:BFO(300 nm)/STO sample measured by atomic force microscopy (AFM). 36
Figure 3.2: Omega scans of a Ba:BFO(300 nm)/STO sample. 37
Figure 3.3: A reciprocal space map of a Ba:BFO(300 nm)/STO sample. 37
Figure 3.4: The ISOLDE facility at CERN, Geneva, Switzerland [28]. 39
Figure 3.5: Decay scheme of ^{57}Fe from parent nuclei ^{57}Co and ^{57}Mn [32]. 40
Figure 3.6: Beam production at ISOLDE [24]. 41
Figure 3.7: The implantation profile of 45 keV ^{57}Mn implanted in BFO at a 30° angle. 42
Figure 3.8: TRIM estimates of the Bi, Fe and O recoil profiles in Mn implanted $BiFeO_3$.....43
Figure 3.9: Emission Mössbauer spectroscopy set-up at ISOLDE, CERN [24]. 44
Figure 3.10: Schematic diagram of the experimental set-up, including electronics, at ISOLDE [24]. 46
Figure 4.1: Mössbauer spectra of the BBFO (94 nm) sample observed at the temperatures indicated. 49
Figure 4.2: Mössbauer spectra of the BBFO (94 nm) sample observed at the temperatures indicated in Figure 4.1 on a smaller vertical scale. 50
Table 4.1: Fit parameters obtained for BBFO sample of 94 nm size at room temperature, where, $B_{distribution}$ is a combination of two sextets. 51
Figure 4.3: The isomer shifts as a function of temperature of the spectral components of the BBFO sample of 94 nm size. 51
Figure 4.4: The quadrupole splitting as a function of temperature of the spectral components of the BBFO sample of 94 nm thickness. 52
Figure 4.5: The site population dependence as a function of temperature of the spectral components of the BBFO sample of 94 nm thickness. 53
Figure 4.6: Mössbauer spectra of the BBFO sample of 300 nm thickness observed at the temperatures indicated. 54
Figure 4.7: Mössbauer spectra of the BBFO sample of 300 nm thickness shown on a smaller vertical scale.....54
Table 4.2: Fit parameters obtained for BBFO sample of 300 nm thickness at room temperature, where, $B_{distribution}$ is a combination of two sextets. 55

Figure 4.8: The isomer shifts as a function of temperature of the spectral components of the BBFO sample of 300 nm thickness. 55
Figure 4.9: The quadrupole splitting as a function of temperature of the spectral components of the BBFO sample of 300 nm thickness. 56
Figure 4.10: The site population dependence as a function of temperature of the spectral components of the BBFO sample of 300 nm thickness. 57
Figure 4.11: Mössbauer spectra of the undoped BFO sample observed at the temperatures indicated where, figures (c) and (d) are on a smaller vertical scale than (a) and (b). 58
Table 4.3: Fit parameters obtained for BFO sample. 58
Table 4.4: Hyperfine parameters obtained for all samples. 59
Table 4.5: Table of Bhf and areal fractional as a function of temperature. 60
Figure 4.12: The plot of normalised B_{hf} as a function of Temperature/700 K for BFO, BBFO (94 nm and 300 nm thickness) and BBFO results of Kim et al. [16] where, the dotted curve is the magnetization curve calculated with the Brillouin function for spin s = 5/2. 61

1 INTRODUCTION

1.1 Background of Bismuth Ferrite (BFO) and requirement for doping

Magnetic and electronic materials infiltrate every aspect of modern technology [1], as seen in the following examples, data is stored as areas of opposite magnetic polarization in ferromagnets which are materials with a spontaneous magnetic polarization that can be reversed by a magnetic field. Sensors use ferroelectrics which are materials with a spontaneous electric polarization that can be switched by an applied electric field. Many ferroelectrics are also ferro-elastic, these display a change in their electric polarization when accompanied by a change in shape. They are used to convert sound waves into electrical signals in sonar detectors and to convert electrical impulses into motion in actuators [1].

The desire to miniaturize devices has led to increased interest in combining electronic and magnetic properties into multifunctional materials so that a single device component can perform more than one task. Materials which combine 'ferroic' and magnetic properties in the same phase, are known as multiferroics [1].

Although, its microscopic origin is a long-standing controversy in the scientific community, a revival of interest developed in the beginning of the 21st century due to the emergence of multiferroic frustrated magnets in which the ferroelectricity is magnetically induced and which present an inherent strong magnetoelectric coupling [2]. Multiferroics are particularly appealing because they exhibit interactions between the magnetic and electric polarizations which lead to additional functionalities such as the magnetoelectric effect which is the induction of a magnetization by an electric field, or of a polarization by a magnetic field, first conjectured by Curie in 1894 [2]. This effect is potentially important for information storage applications as it would allow magnetic information to be written electrically and to be read magnetically [3]. However, attempts to design multiferroics that combine ferromagnetism and ferroelectricity in the same phase have proved unexpectedly difficult [1]. Figure 1.1 schematically illustrates the relationship between an electric field, magnetic field and stress and their effects on ferroic and magnetoelectric multiferroic materials.

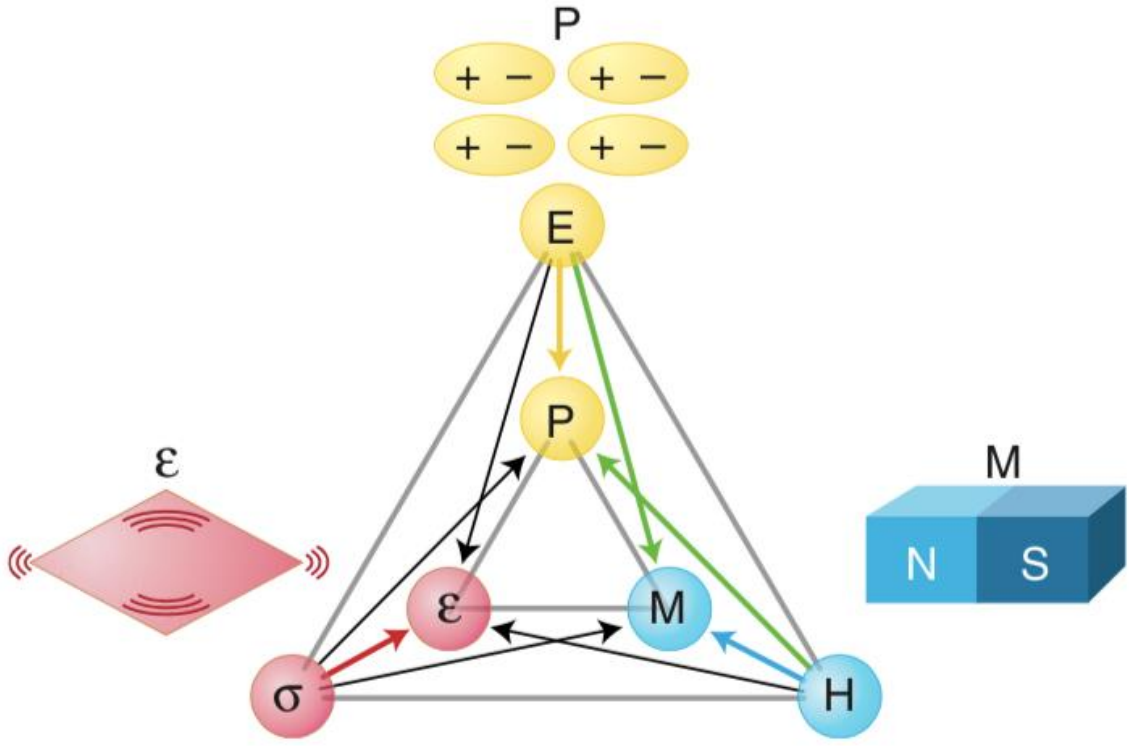

Figure 1.1: The electric field, E, magnetic field, H and stress, σ control the electric polarization, P, magnetization, M, and strain, ε respectively. In a ferroic material, P, M or ε produce ferromagnetism, ferroelectricity or ferroelasticity, respectively. In a magnetoelectric multiferroic, a magnetic field may control P, or an electric field may control M, this is indicated as green arrows [1].

Bismuth Ferrite, $BiFeO_3$ (BFO), is a single-phase multiferroic material with a distorted perovskite structure ABO_3 [4]. It has high ferroelectric Curie (T_C = 1123 K) and Néel temperatures (T_N = 643 K), and therefore, is both ferroelectric and antiferromagnetic at room temperature. Note that the precise value and nature of T_C has been debated [5]. Although BFO is multifunctional, the atomic-level mechanisms driving ferromagnetism and ferroelectricity are mutually exclusive because they require empty and partially filled transition metal orbits, respectively [6]. This apparent incompatibility can be overcome in materials such as BFO, and other ABO_3 structured materials, where the A and B site cations are sources of ferroelectricity and magnetism, respectively [7] - an additional electronic or structural driving force must be present for magnetic and ferroelectric ordering to occur simultaneously [8].

At room temperature, bulk BFO crystallizes in a rhombohedral symmetry with the R3c space group. Ferroelectricity in BFO is driven by the stereo-chemical activity of $6s^2$ lone pair of Bi^{3+} ions, whereas the Fe ions order antiferromagnetically. It is a G-type antiferromagnet with a long-range cycloidal spin arrangement of wavelength 62 nm, disproportionate to the lattice. The saturation polarization in this material can reach as much as 60 $\mu C/cm^2$ in suitably prepared thin films [7]. Sosnowska *et al* [9] studied the BFO magnetic structure and showed that each Fe^{3+} spin is surrounded by six antiparallel spins on the nearest Fe neighbours (G-type anti-ferromagnetism). The exchange interaction between neighbouring Fe magnetic moments is ferromagnetic within the $[001]_h$ planes and antiferromagnetic along $[001]_h$. The R3c symmetry also permits a canting of the antiferromagnetic sub-lattice resulting in a weak ferromagnetism if the magnetic moments of Fe^{3+} are oriented perpendicular to the $[001]_h$ axis. Figure 1.2 presents a schematic view of the R3c structure in the rhombohedral representation [10].

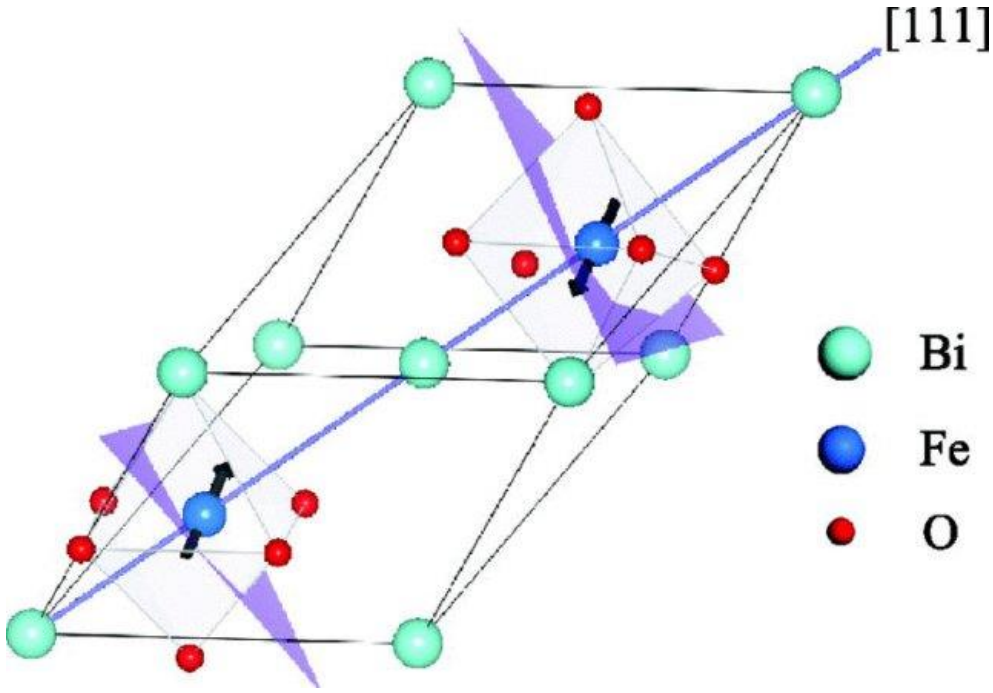

Figure 1.2: Schematic view of the rhombohedrally distorted perovskite structure in the R3c space group representation of bismuth ferrite. The vectors denote the spins of Fe ions [10]. Here, in the ABO_3 phase, Bismuth is placed at the A-site and Iron at the B-site.

Due to this multiferroic behaviour, BFO is seen as a promising future material for oxide memory devices [11]. However, the magnetoelectric coupling in BFO is too weak for many practical applications, reason being that the antiferromagnetic spin configuration in BFO is modified by a long-range modulation leading to a spiral modulated spin structure. This spiral spin structure cancels the macroscopic magnetization and although, they exhibit a quadratic effect, it prevents the observation of a linear magnetoelectric effect.

As a prerequisite for creating BFO based multiferroics exhibiting a strong linear magnetoelectric effect, the spatially modulated structure can be suppressed in a number of ways: application of a strong magnetic field shows that the cycloid spin structure is converted to homogeneous spin order, isovalent substitutions of rare earth ions for bismuth (Bi^{3+}) ions in BFO, heterovalent substitutions of alkaline earth and niobium (Nb^{5+}) ions for Bi^{3+}, growth of thin films based on bismuth ferrite and its derivatives and rare earth doping of BFO increases the spontaneous polarization and magnetization of the forming solid solutions [12].

Doping was considered the best way to enhance the multiferroic property through suppressing its cycloid structure or reducing the second phase, thereby, reducing impurities, large leakage current as a result of oxygen vacancies and antiferromagnetic nature which are an addition of barriers in applications of BFO.

The search for a fundamental understanding of the origin and nature of magnetism in doped BFO is motivated by the possibility of potential technological applications. This dissertation seeks to contribute to this search through focusing on studies of the ^{57}Fe implanted, Barium doped, BFO. ^{57}Fe emission Mössbauer spectroscopy (eMS) was applied in the study, using the short-lived radioactive isotope, $^{57}Mn^*$ with a half-life, $t_{1/2}$ = 1.5 min, as a precursor. Mössbauer spectroscopy has been selected as the main research tool because of its extreme sensitivity to both the bonding mechanism and the local environment in the vicinity of the probe atoms as well as its distinct signatures for paramagnetic, anti-ferromagnetic and ferromagnetic behaviour.

1.2 Literature review of Barium doped Bismuth Ferrite (BBFO)

Multiferroic materials that are simultaneously ferromagnetic and ferroelectric are currently attracting great attention because of the possibility of modulating electrical polarization with a magnetic field and magnetization with an electric field in these materials. These materials can pave the way to new technologies which will exploit both electrical and magnetic polarizations to store and manipulate information [7]. The impurities, large leakage current and anti-ferromagnetic nature are some of the barriers in applications of BFO in addition to evidence proving it is a challenge to prepare single phase BFO by using solid-state reaction at high sintering temperature [7]. The standard solid-state reaction sintering of BFO results in a loss of Bi^{3+}, a high density of oxygen vacancies as well as formation of impurities other than the ABO_3 phase. In order to avoid the Bi^{3+} deficiency and accelerate the kinetics of the chemical reaction between atoms during sintering, a rapid liquid sintering technique has been used by previous researchers. By this sintering method, high quality and singe-phase BFO ceramics can be synthesized [13].

Magnetoelectric effects have been observed in the form of ferroelectric phase transitions induced by magnetic fields in perovskite manganites and ferromagnetism induced by electric fields in hexagonal manganites. However, these single phase multiferroics are not very attractive for short term applications because none of the existing materials combine large electric and magnetic polarizations at room temperature [1].

Originally, the presence of oxygen vacancies led researchers to focus on doping as a tool to reduce the resulting leakage currents in undoped BFO [11]. In order to overcome the previously described barriers, doping was considered the best way to enhance the multiferroic property through suppressing its cycloid structure and reducing any secondary phases. Previous researchers have found that the ferroelectric and magnetic properties of BFO could be improved by substitution such as (Ca^{2+}, Sr^{2+}, Ba^{2+}, Mg^{2+}, Pb^{2+}) cations at Bi^{3+} site and by (Co^{3+}, Cr^{3+}, Mn^{3+}, Ti^{4+}, V^{5+}, Nb^{5+}) cations at Fe^{3+} site. These substitutions lead to a change in crystal symmetry of $BiFeO_3$ [4].

The reason for high leakage current is the existence of Fe^{2+} ions and that of the high density of oxygen vacancies is due to the preferred evaporation of Bi^{3+} and variable Fe^{2+} and Fe^{3+}

during materials sintering [13]. A-site and B-site co-doping is a good way to improve the multiferroic properties of BFO, both in films and ceramics [14]. In principle, both cations, on the A and B sites of the perovskite structure, can be substituted by other metals [11]. It has been a popular strategy to perform A-site doping of BFO by rare-earth ions in order to enhance the polarization and to sinter pure BFO perovskite phase in order to reduce the leakage current [9]. It has been found that doping at the A–site affects the centrosymmetry of the FeO_6 octahedra which creates oxygen vacancies and leads to a change in multiferroic properties of $BiFeO_3$ [4].

In order to develop oxide electronics, doping and the p-n junction are vital [11]. Doping experiments in oxide materials have proven to be complicated by the presence of other defects. This follows from the following facts - oxygen vacancies create *n*-type doping, on the other hand, cation vacancies create *p*-type doping. Thus, controlling the defect chemistry in doped oxides is important. Otherwise, the effects of defects could completely change the desired effects of substitutional doping, since, defect rich materials are prone to low conductivity. As a result, *p*-type substitutional cation doping is challenging and has so far only been reported for Ca^{2+} and Ba^{2+} [11]. Formation energies and the relative energetic positions of the introduced acceptor or donor levels gives insight into the performance of each dopant. This enables researchers to suggest Ba^{2+} as a candidate for doping [11].

The effects of the substitution Ba^{2+} ions on the structural, dielectric, magnetic, ferroelectric and ferromagnetic properties of bismuth ferrite sample as presented in a number of published reports [see, for example, references [2-19]. Magnetic and ferroelectric properties of BFO are found to change with Ba^{2+} ions substitution. Ba doping transformed antiferromagnetic BFO to ferromagnetic material and resulted in enhanced magnetization [4]. The dielectric properties as well as the crystalline structure of the samples of the samples were affected by the Ba^{2+} ions. Abnormal dielectric constant was observed. This suggests the coupling between the magnetic and dielectric properties. These results suggest that the BBFO nanoparticles are a good candidate for data storage applications. Finally, the simultaneous occurrence of ferromagnetic and ferroelectric hysteresis loops in BBFO multiferroic nanoparticles system at room temperature makes it a potential candidate for information storage and spintronic applications [4].

$Bi_{1-x}Ba_xFeO_3$ (0.0 < x < 0.25) ceramics were prepared following a chemical synthesis route [15]. It was found that doping with lone-pair active ions at A-sites and magnetic transition metals at B-sites reduced the leakage current in BFO [15] as well as changed the cycloidal spin structure of BFO to a canted spin structure [13] which could be the reason behind the enhancement in magnetic properties in doped samples [15]. Magnetic and ferroelectric properties of BFO were found to change significantly with Ba substitution in place of Bi. Above the Néel temperature of pure BFO, a large enhancement in magnetization was observed in Ba doped samples. Magnetic and ferroelectric transition temperatures shifted towards higher temperature with the increase in dopant concentration. Canting of spins and displacement of oxygen atoms from their original position could be the reasons for enhanced magnetic and ferroelectric properties, respectively. A noticeable change in dielectric constant with doping and the observed change in lattice parameters indirectly confirm that the Ba ion is not remaining isolated in the compound but enters the lattice. Magnetoelectric coupling also increases due to Ba substitution [15].

Ba doped $BiFeO_3$ compounds have also been prepared via a solid-state reaction [6]. Adding Ba^{2+} ions to BFO requires charge compensation, which can be achieved by formation of Fe^{4+} or oxygen vacancies. If Fe^{4+} exists, the statistical distribution of Fe^{3+} and Fe^{4+} ions in the octahedra may also lead to net magnetization and ferromagnetism [6]. Ba substitution has not affected the crystalline structure of the parent compound BFO. This is important for keeping ferroelectric properties in $Bi_{1-x}Ba_xFeO_3$ [6]. The change in the dielectric constant with applied magnetic field suggests that magnetoelectric coupling exists in this compound [6]. X-ray diffraction showed that $Bi_{1-x}Ba_xFeO_3$ was single phase up to x = 0.25. These samples exhibited magnetism and ferroelectricity simultaneously at room temperature [6].

Interestingly, divalent cation (A) substituted $Bi_{0.7}A_{0.3}FeO_3$ (A = Ca, Sr, Pb, and Ba) also exhibit enhanced magnetization [7]. The magnetic-field induced ferroelectric hysteresis loop in $Bi_{0.75}Sr_{0.25}FeO_3$ makes it more attractive for practical applications. It was found that the divalent cation doping in the anti-ferromagnetic $BiFeO_3$ enhances the magnetization and results in a well-developed hysteresis loop. The magnitude of the spontaneous magnetization increases with the size of the dopants [7].

Ba^{2+} doped BFO was synthesized using a sol-gel method [19]. The spontaneous magnetization in BFO could be induced by changing the Fe-O-Fe bond angle or by statistical octahedral distribution of Fe [19]. Ba^{2+} doping in A site was observed to improve multiferroic properties of BFO. Substituting Ba^{2+} in BFO distorts its original structure due to larger ionic radii of Ba and changes its cycloidal spin structure to a canted spin structure resulting in the magnetization at room temperature. Also, addition of Ba^{2+} in BFO is believed to reduce the oxygen vacancy related defects significantly which in turn improves the electrical properties [6]. Ba^{2+} substitution leads to the increase in the unit cell volume. The separation between (104) and (110) diffraction peaks are reduced with Ba substitution which may imply that the rhombohedral structure might have distorted to either tetragonal or monoclinic structure [8]. These structural changes with Ba^{2+} doping in BFO might be an important factor considered for ferroelectric properties of these materials [19]. The magnetization was observed to be enhanced with the increase of Ba^{2+} concentration up to x = 0.2 and with the further increase to x = 0.3, the magnetization was lowered. The enhancement of magnetization with Ba^{2+} concentration was previously observed [19]. The enhanced magnetization in this case was attributed to the suppression of spin spiral structure of BFO and due to the replacement of Bi^{3+} ions by Ba^{2+} ions in the lattice site, in which the system was destabilized by creating the charge imbalance. In this process, one oxygen vacancy will be created for every two alkaline metals to stabilize the system. This suppression of spiral spin structure by the oxygen vacancy enhances the ferromagnetism in Ba^{2+} substituted BFO [19].

$Bi_{0.74}Ba_{0.30}FeO_3$ and $Bi_{0.74}Ba_{0.30}Fe_{0.95}Ti_{0.05}O_3$ ceramics were synthesized by a tartaric acid modified sol–gel method [18]. Ba doping significantly enhanced the room temperature anti-ferromagnetism which was generally attributed to the structural modification, leading to the suppression of canted spin structure or the valence fluctuation of Fe ions. It has been reported that the structure of $Bi_{1-x}Ba_xFeO_3$ changed from rhombohedral to tetragonal with x up to 0.20. However, neutron diffraction results have confirmed that the magnetic structure of tetragonal $BiFeO_3$ system is collinear G-type anti-ferromagnetism which means that the macroscopic magnetism will be very weak. Thus, the origin of enhanced ferromagnetism in Ba doped $BiFeO_3$ has not been decided [18]. In this work, the authors reported the preparation and the ferroelectric, ferromagnetic and magnetoelectric properties of the Ba doped BFO ($Bi_{0.75}Ba_{0.25}FeO_3$) thin films on Pt/TiO_2 /SiO_2 /Si(1 0 0) substrates by pulsed laser

deposition [17]. They reported Ba doped BFO, $Bi_{1-x}Ba_xFeO_3$ ($x < 0.3$), which exhibits ferroelectric, ferromagnetic properties and magnetoelectric effects at room temperature. In this study, Ba content of $x = 0.25$ was found to be the optimal doping concentration to show the best properties of this material. To explore the properties and the potential application of this new multiferroic material, fabrication of thin films of this material is necessary. The Si substrate is of particular importance in device application, particularly in incorporating into integrated circuits [17].

The quest for robust room temperature ferromagnetic ferroelectrics that are sufficiently insulating to sustain a large macroscopic polarization is a major challenge. Finally, advances in fundamental theoretical concepts should lead to a more concise picture of the different forms of ferroic ordering and the relations between them. This should result in a better understanding of the physics of multiferroics [1].

1.3 Aims and Objectives of the study

The broad aim of the present study is to investigate the hyperfine interactions of ^{57}Fe probe ions implanted in Barium doped Bismuth Ferrite (BBFO) as well as in undoped BFO from experimental investigations as a function of annealing temperature. As highlighted in the introduction, emission Mössbauer spectroscopy (eMS) in which the 14.4 keV Mössbauer state in ^{57}Fe was populated by β-decay of radioactive ^{57}Mn, was employed at ISOLDE/CERN to investigate the magnetic properties of BBFO samples.

These studies were conducted utilising online eMS measurements at ISOLDE, CERN within experiment **IS630** with the Emission Mössbauer Collaboration, using short- lived radioactive $^{57}Mn^*$ ($t_{1/2} = 1.5$ min) with extremely low fluences, $\sim 3 \times 10^{12}$ ions/cm^2 ($\sim 10^{-4}$ at. %) implanted in BBFO. Temperature dependent eMS measurements were carried out in the temperature range of 300-660 K. Preparation of the samples and their characterization were conducted by Sven Becker and Gerhard Jakob at the Institute of Physics, Johannes Gutenberg University Mainz, Germany.

The present study therefore had the following objectives, to:

- determine the lattice location and chemical nature of Fe impurity atoms in different lattice sites of BBFO compound semiconductors,
- determine the isomer shifts and quadrupole splitting values and area fractions of Fe impurities at the different lattice sites and in impurity complexes,
- determine charge states of Fe impurities in different sites (based on values of isomer shifts and quadrupole splitting),
- investigate the annealing behaviour of the radiation damage as a function of annealing temperature,
- determine the nature and origin of magnetism in BBFO and compare with previous studies,
- and establish if vacancies/interstitials/complexes are created during the implantation.

The principles of the Mössbauer Effect are presented in Chapter 2 where the hyperfine interaction parameters that allow the effect to be used as a sensitive tool are also discussed. Experimental details of the measurements following ^{57}Mn* implantation at the on-line isotope separator facility, ISOLDE, are presented in Chapter 3. The results are presented and discussed and compared with rare earth doped and undoped $BiFeO_3$ systems [27] in Chapter 4, and conclusions drawn from the investigations are presented in Chapter 5.

2 THEORY

2.1 The Mössbauer Effect

In 1957, whilst working on his doctoral thesis in Heidelberg, Rudolf L. Mössbauer discovered the recoilless nuclear resonance absorption of gamma-ray photons which became known as the Mössbauer Effect and earned him the Nobel Prize in Physics in 1961 [20]. Mössbauer discovered the effect in Iridium-191, but with the discovery of the effect in ^{57}Fe by Stanley Hanna [21], the phenomenon rapidly developed to a new spectroscopic tool for the study of a range of chemical and physical systems. This practical new method led to an avalanche of research activity employing Mössbauer Spectroscopy as a very sensitive interrogation tool. Even though the Mössbauer effect has been detected in almost 50 different elements and 100 different nuclides, only a few of these elements are widely used as Mössbauer effect probes [22]. Among these isotopes, ^{57}Fe is the easiest, most informative, most widely used nuclide [23] and is focused on in the present work. ^{57}Fe is the most important Mössbauer nuclide although it has a natural abundance of only 2.2%. The half-life of its 14.41 keV excited state is 98.3 ns. As a result, the resolution of ^{57}Fe Mössbauer spectroscopy, given by the ratio of the linewidth to the γ-ray energy, is 6.5×10^{-13}, - making it an exceptionally sensitive probe.

This effect provides a way of probing the local environments of particular atoms in amorphous or crystalline solids. Widespread information on the electronic, magnetic and geometric structure of an impurity atom environment can be extracted from the parameters that characterize the Mössbauer spectra resulting from hyperfine interactions. The following section consists of a detailed discussion of the hyperfine interactions between nuclei and electrons and the Mössbauer parameters which allow the effect to be applied as an analytical tool.

2.2 Factors contributing towards the Mössbauer effect

2.2.1 Nuclear resonance fluorescence

The properties of the nuclear transition and of the emitted gamma-ray by a nucleus are coupled by the conservation of energy and momentum involved during the resonance emission of the gamma-rays [22]. When a free, excited nucleus of mass *m* with *Z* protons and *N* neutrons decays to the ground state by emitting a gamma-photon, the emitted photon

carries away energy, E_γ, as well as momentum $p_\gamma = E\gamma/c$ a result of the conservation of momentum. Consequently, the energy carried by the gamma-ray is the transition energy, E_O but lessened by the value of the recoil energy, E_R. This forbids subsequent resonant absorption of the gamma-ray by another identical nucleus as illustrated in Figure 2.1. The emitted gamma-ray can be absorbed by another identical nucleus if both processes are recoilless [22]. The absorption can only occur for a nucleus in the ground state, hence, a gamma-ray emitted in a transition to the ground state is useful for practical application of the Mössbauer effect [22, 26].

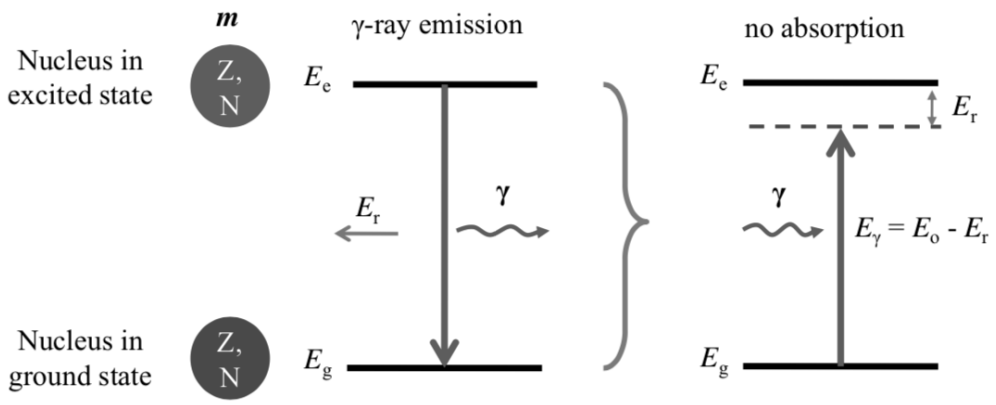

Figure 2.1: Non-resonant gamma-ray absorption as a result of loss in energy as recoil energy [24].

When a nucleus is bound in a crystal lattice with a mass M that is much greater than the nucleus mass *m*, the loss in energy due to recoil becomes insignificantly small [22]. Hence, recoil free emission of the gamma-ray occurs. This is the fundamental principle of the Mössbauer effect. In this instance, the energy of the gamma-ray is equivalent to the transition energy between the ground state and the excited state then resonant emission and absorption by another identical nucleus bound in a crystal lattice can occur as seen in Figure 2.2 [22].

The nucleus remains in the excited state of energy, E_0 for the mean lifetime after the absorption process and then undergoes a transition back to the ground state by emission of

either a gamma-ray or conversion electrons due to internal conversion in which part of the photon energy is transferred to an electron in the innermost electron shells of the atom. This process is referred to as *nuclear resonance fluorescence* [22].

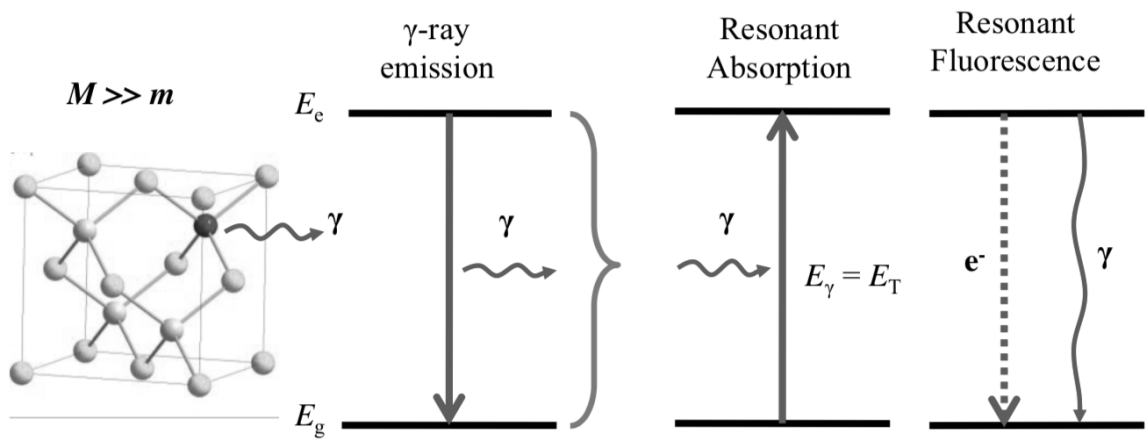

Figure 2.2: Resonant emission and absorption of gamma rays between nucleii and resonance fluorescence and conversion electrons [24].

2.2.2 Recoil energy

A gamma-ray emitted from an excited nucleus of mass M which is initially at rest carries away both energy E_γ and momentum $p_\gamma = E_\gamma/c$, as illustrated in Figure 2.3 below. As a consequence, the nucleus recoils in the opposite direction with an energy E_R, given by

$$E_R = \frac{1}{2}Mv^2 = p_\gamma \tag{2.1}$$

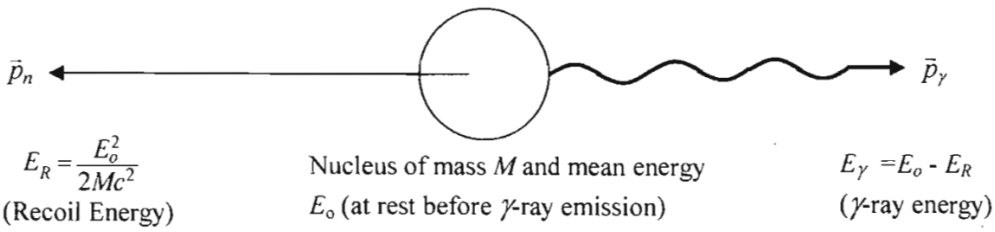

Figure 2.3: Effect of recoil on a nucleus of mass M and resulting energies [27].

By the conservation of momentum, the above process gives

$$p_M = -p_\gamma = -\frac{E_\gamma}{c}, \tag{2.2}$$

where, p_M and p_γ are the linear momenta of the nucleus and the gamma-ray, respectively [22, 30]. Using non-relativistic approximations and considering the large mass of the nucleus Eq. (2.2) gives

$$E_R = \frac{{p_M}^2}{2M} = \frac{{E_\gamma}^2}{2Mc^2}. \tag{2.3}$$

For $E_R \ll E_o$, let $E_\gamma \approx E_o$ in the above equation so that

$$E_R = \frac{{E_O}^2}{2Mc^2} \tag{2.4}$$

which results in $E_R(\mathrm{eV}) = 5.37 \times 10^{-4} \frac{{E_O}^2\,(\mathrm{keV})}{A}$ where A is the mass number of the decaying nucleus. For ^{57}Fe, $E_O = 14.4$ keV, hence, $E_R = 1.95 \times 10^{-3}$eV [22, 26].

2.2.3 Recoil-free fraction

In the case of the nucleus being fixed in a lattice, the recoil energy can be transferred to lattice vibrations in the vicinity of the probe atoms, hence, the energy of the gamma-ray may cause excitation of a lattice vibrational mode causing a decrease in the energy of the emitted photon [22, 31 -33]. There are *3N* vibrational modes in an Einstein model each of frequency, ω_E. Only the transfer of integral multiples of quantized phonon energy that is proportional to this frequency in the lattice permits the emission and absorption of a gamma-ray [26, 30].

For the case of $E_R \ll \hbar\omega_E$, a portion of gamma-ray photons can be emitted without loss of energy to nuclear recoil. These are transitions which take place without excitation of lattice vibrations, the so-called *zero phonon vibrations*. The fraction of this emission with zero phonon excitation is known as the recoil-free fraction, f or the Mössbauer-Lamb factor,

$$f = \exp\{-k^2 \langle x^2 \rangle\}, \tag{2.5}$$

where, $\langle x^2 \rangle$ is the mean square vibrational amplitude of the emitting or absorbing nucleus along the direction of the emitted gamma-ray wave vector k [26, 30]. The probability of a recoil-free transition then decreases exponentially with the square of the gamma-ray energy. It is defined as the number of recoil-free gamma emission or absorption events divided by the total number of gamma events.

In other cases, the Debye model is not limited to single vibration frequencies of lattice atoms. Instead, it entails a continuum of oscillator frequencies [26, 30]. For a Debye model approximation which is valid for cubic monatomic crystals, f is given by

$$f = \exp\left\{-\frac{3}{2}\frac{E_\gamma}{k_B\,\theta_D}\left[1 + 4\left(\frac{T}{\theta_D}\right)^2 \int_0^{\frac{\theta_D}{T}} \frac{x}{e^x - 1}\,dx\right]\right\}, \tag{2.6}$$

where k_B is the Boltzmann constant and θ_D is the Debye temperature. θ_D is a measure of the bond strength between the Mössbauer probe atoms and the nearest neighbouring atoms in the crystal lattice [22, 31-33] given by

$$\theta_D = \frac{hw_D}{k_B}. \tag{2.7}$$

When, $T \ll \theta_D$

$$f = \exp\left\{-\frac{E_R}{k_B\,\theta_D}\left[\frac{3}{2} + \frac{\pi^2 T^2}{\theta_D}\right]\right\} \tag{2.8}$$

and in the high temperature limit of, $T \geq \theta_D$

$$f = \exp\left\{-\frac{6E_R T}{k_B\,\theta_D}\right\}. \tag{2.9}$$

The recoil-free fraction depends on the recoil free energy, lattice properties and ambient temperature. f is a measure of the probability of recoil-free resonance fluorescence of gamma-photons. Therefore, f will tend to be larger when the probability of exciting the lattice vibration is small, which means lower gamma-ray energy. As the binding energy of the atom gets stronger in the lattice, the temperature reduces as the vibrational energy gets lower. Therefore, the Mössbauer effect can be detectable in solids and viscous fluids as the

displacement of the nucleus must always be small compared to the wavelength of the gamma-ray [22, 26, 30-33].

2.2.4 Natural line width

According to Heisenberg's Uncertainty Principle, a nuclear level with a mean lifetime, τ_N, has an energy uncertainty, Γ, given by

$$\Gamma = \frac{\hbar}{\tau_N} \tag{2.10}$$

where, Γ is the natural line width which is taken as the full width at half maximum (FWHM) of the Lorentzian line shape of the spectral line [26, 30].

2.2.5 Spectral line shape

In Mössbauer spectroscopy, the lifetime of excited states varies from $\sim 10^{-6}$ to 10^{-11} s. For the ^{57}Fe Mössbauer state, which has an energy transition of $14.4\ \mathrm{keV}$ and a mean lifetime of $141\ \mathrm{ns}$, the resulting value for the linewidth τ is $4.55 \times 10^{-9}\ \mathrm{eV}$ [22, 26]. Maximum resonance only occurs when the spectral line for emission and absorption appears at the same energy position [22]. Therefore, the gamma emission probabilities as a function of the transition energy, $I(E)$, yield spectral lines centered around the nuclear transition energy, E_0, where E_0 is the mean energy of the transitional probability [22, 34-35] . The Lorentzian line shape as seen in Figure 2.4 is described by the Breit-Wigner formula,

$$I(E) = \frac{\left(\frac{\Gamma}{2}\right)^2}{(E - E_0)^2 + \left(\frac{\Gamma}{2}\right)^2} \tag{2.11}$$

where Γ is the natural linewidth of the spectral line, $I(E)$ is the transition energy intensity, E is the transition energy and E_0 represents the most probable transition energy [22, 34-35].

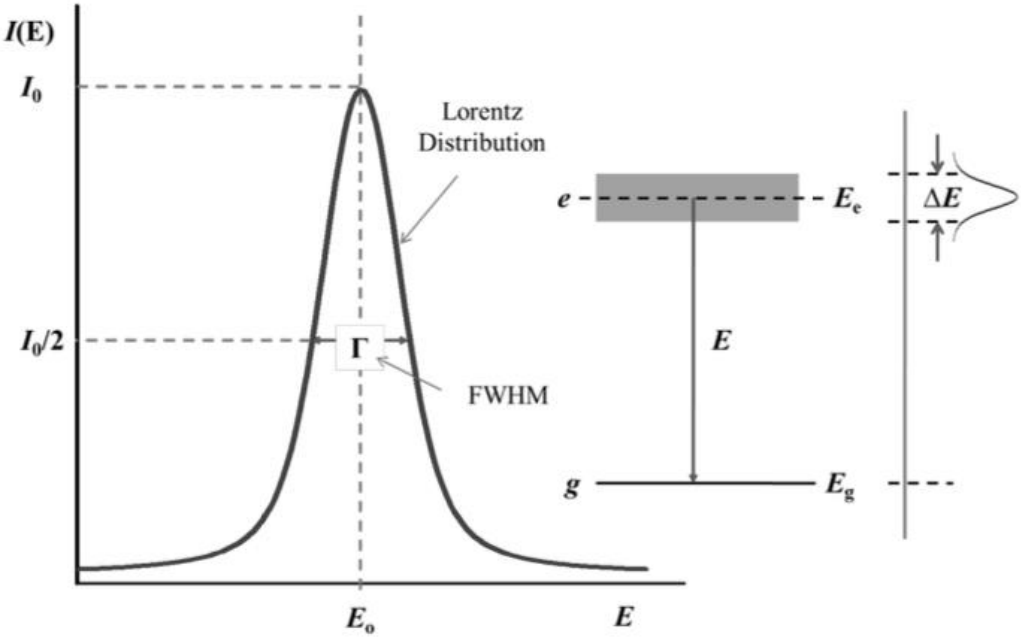

Figure 2.4: Intensity distribution for gamma-ray emission dependent on transition energy E_0 where e is the excited state and g is the ground state [24].

2.3 Mössbauer spectra

The detection of resonant absorption by a stable nucleus of an isotope of the probe nucleus, in a suitable absorber material, of gamma-radiation emitted in the transition of an excited state to the ground state of the radioactive probe nucleus, which is in the source, is recorded to produce a Mössbauer spectrum [22, 26] . The resonant absorption is detected by a change in the counts at the resonant velocities in backscattering geometry or transmission geometry, respectively. A gamma-ray with variable energy is required to observe resonance between the source and the absorber. This is achieved by vibrating the detector, which is the absorber, relative to a stationary source, which is the sample. In this way, the gamma-ray energy is controlled by the Doppler effect in emission Mössbauer spectroscopy [29]. In the case of ^{57}Fe, a velocity drive of 1 mm s^{-1} corresponds to an energy change of 4.80766(3) x 10^{-8} eV [42].

The intensity of the gamma-radiation transmitted is measured as a function of drive velocity (in $\mathrm{mm\,s^{-1}}$) of the source or absorber. The amount of resonant absorption at various velocities is determined by how much of the shifted absorption energy profile overlaps with the relatively stationary emission energy profile spectrum as shown in Figure 2.5 (a). The

greater the overlap, the higher the intensity of the resonant absorption line as illustrated in Figure 2.5 (b) which shows the development of an emission Mössbauer spectrum as the absorber is moving from negative to positive velocities relative to the stationary source [22, 26].

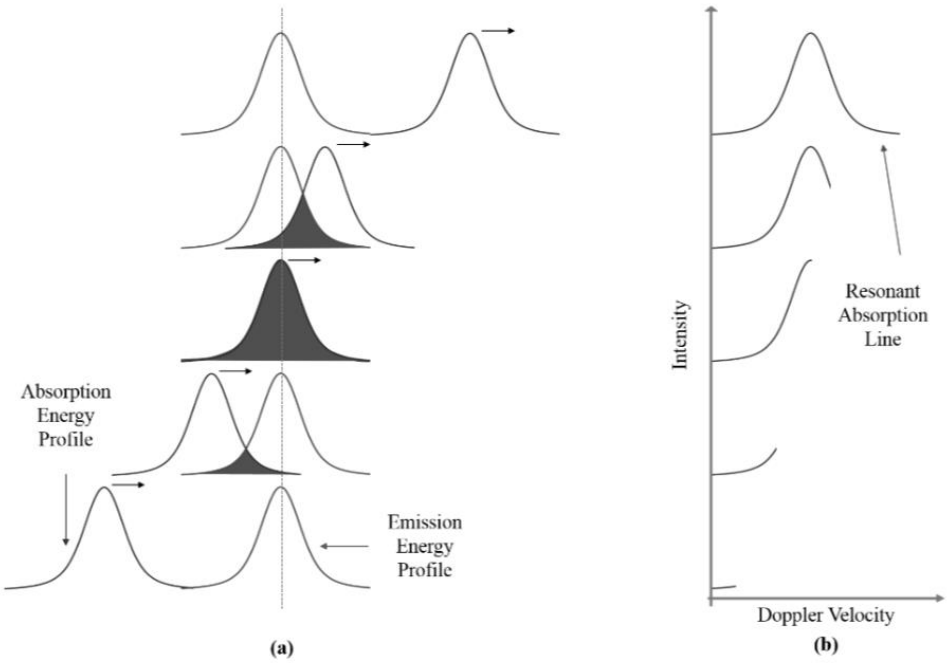

Figure 2.5 : The development of an emission Mössbauer spectrum, as presented in ref. [24].

The velocities for resonant absorption and shape of the spectrum are determined by the combined effect of the hyperfine interactions at site of the Mössbauer probe atoms, which depend on the charge density and distribution in their immediate environments [22, 26]. The Mössbauer effect, thus, relates the probe nucleus with its nearest neighbours through the hyperfine interactions which are discussed in section 2.4. The typical ^{57}Fe hyperfine parameters are of the order of a few millimeters per second and range up to many times the natural linewidth of 0.097 mm s^{-1}, hence, they are easily measured with excellent resolution [23].

2.3.1 Relative intensities of resonance lines in Mössbauer spectra

The line intensities of the hyperfine components in Mössbauer spectra are determined by the theory of the coupling of angular momenta, given that the quadrupole splitting, magnetic

splitting and the spin quantum numbers for each state are known [22, 26]. Line intensities are also known as nuclear transition probabilities which consist of angular independent and angular dependent terms and are given by the square of the corresponding Clebsch-Gordan co-efficients, C,

$$P(\langle I_1 J - m_1 m \mid I_2 m_2 \rangle) \propto |\langle I_1 J - m_1 m \mid I_2 m_2 \rangle|^2, \tag{2.12}$$

where I_2 and I_1 are nuclear spins of the excited and ground states, respectively, J is the vector sum $I_1 + I_2$ and also referred to as the multi-polarity of the transition, m_1 and m_2 are quantum numbers, m is the vector sum $m_1 - m_2$ [22, 25-26].

If there is no change in polarity during the decay the transition is classified as the magnetic dipole (M1) or electric quadrupole (E2) [27]. The majority of Mössbauer isotopes decay by dipole or quadrupole transitions. The multipolarities of the transitions are summarized below in Table 2.1.

Table 2.1: Classification of multipoles in electromagnetic transitions [27].

Multipolarity of transition	π_y	***Notation***	***Transition***
1	+1	M1	Magnetic dipole
1	-1	E1	Electric dipole
2	+1	E2	Electric quadrupole
2	-1	M2	Magnetic quadrupole

For ^{57}Fe, of the eight possible transitions due to the absorption transition, $\frac{1}{2} \rightarrow \frac{3}{2}$, the transitions $+\frac{3}{2} \rightarrow -\frac{1}{2}$ and $-\frac{3}{2} \rightarrow +\frac{1}{2}$ have zero probability as $\Delta m = \pm 2$ for these transitions. The Clebsch-Gordan coefficients of the allowed are listed in Table 2.2. .

The angular-dependent term $\theta(J,m)$ in Table 2.2 is the radiation probability in the direction at an angle θ to the quantization axis. Here, the ratio of line intensities will be $3{:}\,x{:}\,1{:}\,1{:}\,x{:}\,3$, where $x = 4\left(\frac{\sin(\theta^2)}{1+\,cos^2\theta}\right)$.

In Table 2.2, C is calculated by

$$\langle\frac{1}{2}1{-}\boldsymbol{m_1}\boldsymbol{m}|\frac{3}{2}\boldsymbol{m_2}\rangle \tag{2.13}$$

and converted following the relationship given by

$$\langle\frac{1}{2}1{-}\boldsymbol{m_1}|\frac{3}{2}\boldsymbol{m_2}\rangle = (-)^{\frac{1}{2}\boldsymbol{m_1}}\sqrt{\langle\frac{3}{2}\frac{1}{2}\boldsymbol{m_2}\boldsymbol{m_1}|1\boldsymbol{m}\rangle}. \tag{2.14}$$

Table 2.2(a): Relative probabilities for a dipole 3/2→ 1/2 transition. C^2 and $\boldsymbol{\Theta}$ are normalized angular independent and dependent terms. [25].

$\boldsymbol{m_2}$	$-\boldsymbol{m_1}$	$\boldsymbol{m}$	$\boldsymbol{C}$	$\boldsymbol{C^2}$	$\boldsymbol{\Theta}$	$Intensity = \boldsymbol{C^2} * \boldsymbol{\Theta}$	$Relative\ intensity$
$+\frac{1}{3}$	$+\frac{1}{2}$	$+1$	1	3	$1+cos^2\theta$	$3(1+cos^2\theta)$	3
$+\frac{1}{2}$	$+\frac{1}{2}$	0	$\sqrt{\frac{2}{3}}$	2	$2sin^2\theta$	$4(sin^2\theta)$	$\frac{4(sin^2\theta)}{1+cos^2\theta}$
$-\frac{1}{2}$	$+\frac{1}{2}$	-1	$\sqrt{\frac{1}{3}}$	1	$1+cos^2\theta$	$1+cos^2\theta$	1
$+\frac{1}{2}$	$-\frac{1}{2}$	$+1$	$\sqrt{\frac{1}{3}}$	1	$1+cos^2\theta$	$1+cos^2\theta$	1
$-\frac{1}{2}$	$-\frac{1}{2}$	0	$\sqrt{\frac{2}{3}}$	2	$2sin^2\theta$	$4(sin^2\theta)$	$\frac{4(sin^2\theta)}{1+cos^2\theta}$
$-\frac{3}{2}$	$-\frac{1}{2}$	-1	1	3	$1+cos^2\theta$	$3(1+cos^2\theta)$	3

There are two electric quadruple (E2) |3/2> → |1/2> transitions, $\pm\frac{1}{2} \rightarrow \pm\frac{1}{2}$ and $\pm\frac{3}{2} \rightarrow \pm\frac{1}{2}$, whose Clebsch-Gordan coefficients and angular-dependent coefficients are listed in able 2.2 (b).

Table 2.2(b) Clebsch-Gordan and angle-dependent coefficients for Electric Quadrupole 3/2 → ½ transitions.

Quadrupole (E2) Transition	C^2	Θ	***Relative intensities at***	
			$\theta = 90°$	$\theta = 0°$
$\pm\frac{1}{2} \rightarrow \pm\frac{1}{2}$	1	$2 + 3cos^2\theta$	5	2
$\pm\frac{3}{2} \rightarrow \pm\frac{1}{2}$	1	$3(1 + cos^2\theta)$	3	6

The relative transition intensities are 1:3 if the gamma-ray axis is parallel to the direction of Vzz and 5:3 if perpendicular to Vzz.

If the both magnetic and quadrupole interactions are present, then the energy states are represented as a linear combination of terms.

2.4 Relaxation effects on Mössbauer spectra

Time dependent fluctuations of the hyperfine interactions alter the environment of the probe nucleus over its lifetime causing a change in the frequency of the Mössbauer radiation. This phenomenon is known as relaxation [22]. The magnetic hyperfine field sensed at the nucleus of a magnetic ion originates from the electron spin of that ion and the electron spins are coupled to the lattice it is bound within via spin-lattice interactions. As a result, when a disturbance in the electron spin is created, it is propagated throughout the lattice and fluctuations in the magnetic hyperfine field are experienced at the nucleus [29]. Relaxation phenomena play an important role in the interpretation of the experimental results in section 4.

There are two timescales to consider during relaxation, namely, the relaxation time, τ_R which is the average time period between changes of the magnetic hyperfine field, and the lifetime of the ^{57}Fe Mössbauer state which is $\tau_N = 141.8\ \mathrm{ns}$. Furthermore, the relaxation time of the event, τ_R, should be much greater than τ_N so that the magnetic hyperfine fields are detectable in Mössbauer spectroscopy [29].

When $\tau_R \gg \tau_N$, slow relaxation occurs as the magnetic hyperfine field is static during a Larmor precession period and the nucleus experiences each spin state separately. This results in a narrow spectral line which has Lorentzian line shape. It can be seen in Figure 2.6 a, b and c that the spectral lines consist of sextets with narrow lines for spin states of $S_z = \pm \frac{1}{2}$.

For the case of, $\tau_R \ll \tau_N$, fast relaxation occurs as no magnetic interaction is observed because the nucleus experiences a zero-time average of the electron spin. This condition is characterized by the spectra in Figure 2.6 d, e and f where it is observed that individual lines become broader and the spectra cannot only be described by six Lorentzian lines.

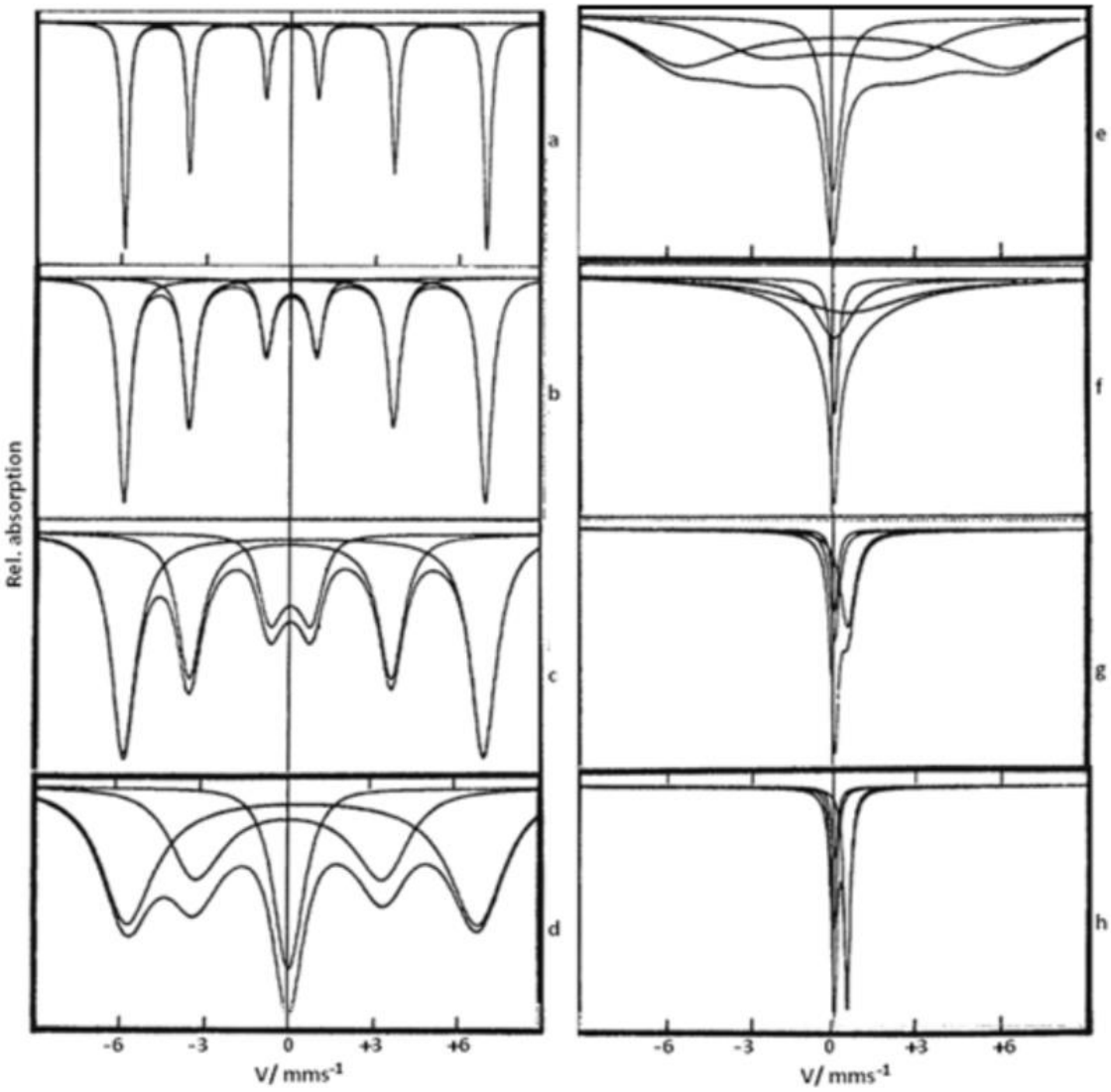

Figure 2.6: Theoretical ^{57}Fe Mössbauer relaxation spectra for longitudinal relaxation [29].

For the case of $\tau_R \approx \tau_L$, the spin relaxation is neither too long nor too short compared to the precession time. Hence, complex spectra with broadened line shapes are observed. In this case, the magnetic splitting collapses to zero for spin state $S_z = 0$ as seen in Figure 2.6 h.

Broadening of the spectral lines is the first effect of relaxation observed when a long relaxation time decreases with increasing temperature. The broadening, $\Delta\Gamma$, of the spectral line-width can be written as

$$\Delta\Gamma = \frac{2\hbar c}{E_0}\,{\tau_R}^{-1} \tag{2.15}$$

where ${\tau_R}^{-1}$ is the relaxation rate, $\hbar c = 197.32697\ \mathrm{eV \cdot nm}$ and $E_0 = 14.4\ \mathrm{keV}$ [29].

2.4.1 Paramagnetic relaxation

It should be noted that there are more conditions, other than those mentioned in section 2.4, that contribute towards fast or slow relaxation times. The system should cater for the entire lifetime of the excited nuclear state, which would include the nuclear spin-spin relaxation, super-paramagnetic relaxation, electronic spin-lattice relaxation and other factors as shown in Figure 2.7. Two of these types that are most relevant to this study are further discussed in sections 2.4.1.1 and 2.4.1.2 following from the fact that the electronic spin relaxation of a probe ion incorporated in a lattice proceeds through two processes [29].

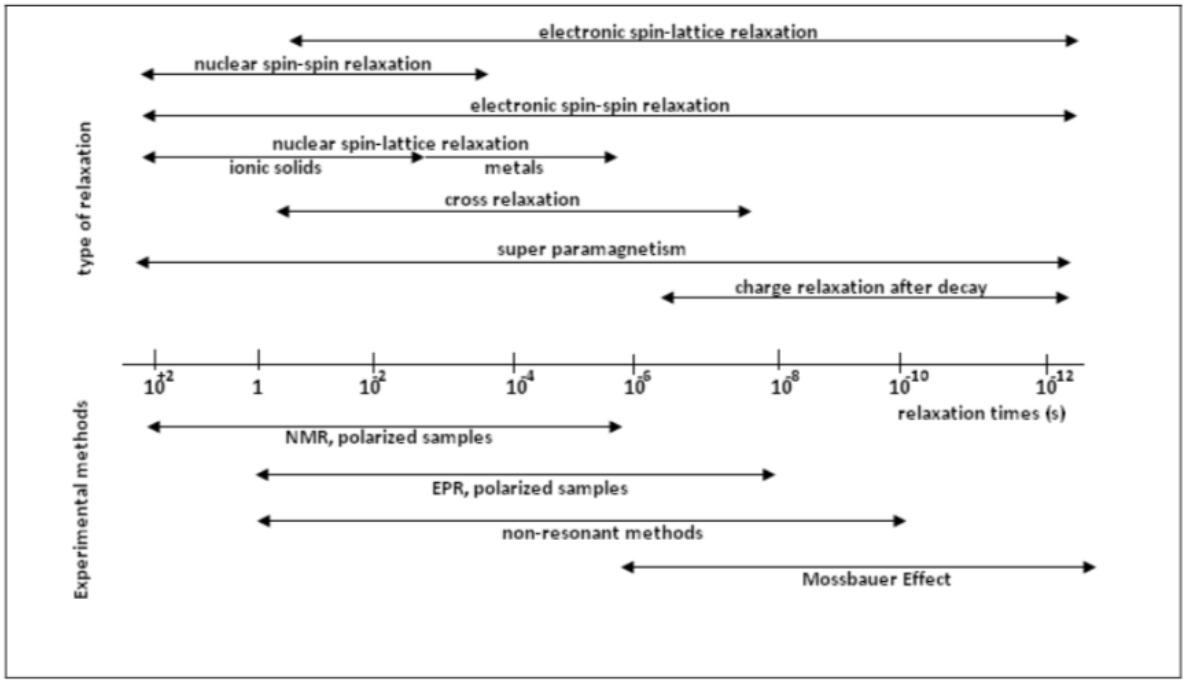

Figure 2.7: Scale of relaxation times [26].

2.4.1.1 Electronic spin-lattice relaxation

Spin-lattice relaxation processes can be exclusively studied in samples with a low concentration, $< 10^{-2}\ at.\%$, of paramagnetic ions because this results in a disappearance of the spin-spin relaxation. The spin-lattice relaxation measures how rapidly or slowly the spins return to their orientation in the longitudinal direction. It depends on the coupling strength to the lattice and involves energy transfer between the electronic spin of the ions and phonons of the lattice vibrations through the spin-orbit interaction and the weaker magnetic dipolar interaction. This relaxation is temperature dependent because of the temperature

dependence of the population of the phonon states which results in a decreased spin-lattice relaxation time with increasing temperature [26, 36-37].

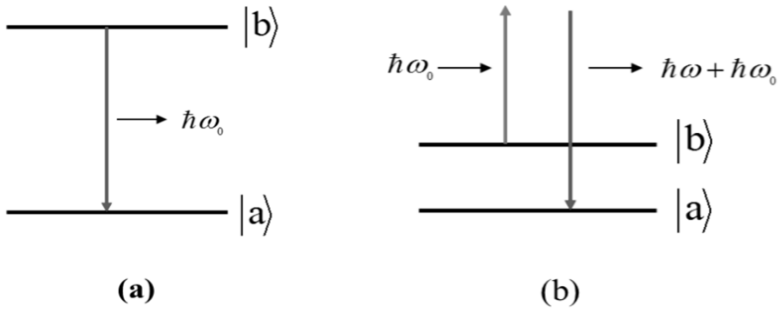

Figure 2.8: Processes that contribute to spin-lattice relaxation - (a) Direct process and (b) Raman process.

Theoretical predictions of the temperature dependent spin-lattice relaxation involve different processes in different temperature ranges relative to the Debye temperature. Figure 2.8 depicts the different processes that contribute towards the spin-lattice relaxation. At low temperatures only low energy phonons contribute. Hence, the direct process dominates in which a spin transition is associated with the creation or total destruction of a single phonon and a linear temperature dependence is seen where, ${\tau_R}^{-1} \propto T$ [29].

At higher temperatures the two-phonon Raman process dominates. The Debye approximation, ${\tau_R}^{-1}$ can be described by,

$$ {\tau_R}^{-1} \propto \left(\frac{T}{\theta_D}\right)^n \int_0^{\frac{\theta_D}{T}} \frac{x^{n-1}e^x}{(e^x-1)^2}dx \qquad (2.16) $$

where n is an integer depending on the process occurring. For temperatures T $> \frac{\theta_D}{3}$, all Raman processes are expected to follow a ${\tau_R}^{-1} \propto T^2$ temperature dependence [26, 36-37].

2.4.1.2 Electronic spin-spin relaxation

This temperature independent relaxation process encompasses an energy transfer between neighboring spins through the magnetic dipole and exchange interactions. This process

depends on the concentration of paramagnetic ions in the sample. This is because the relaxation is mainly produced by magnetic dipole interactions between paramagnetic ions in the sample and the dipole interaction is dependent on the distance between the ions. Hence, increased concentration of the sample decreases the relaxation time.

The concentration of Mn/Fe implanted into the samples in this study is below $10^{-3}\ at.\%$, therefore, the spin-spin relaxation process is considered negligible as the ions are widely spaced [29].

2.5 Hyperfine interaction parameters

The number, shape, position and relative intensity of the various absorption lines characterize a Mössbauer spectrum. These features result from the nature of the hyperfine interactions. The hyperfine interactions give a direct measure of these very small perturbations of the nuclear energy levels. These energy fluctuations are sensitive to changes in the structure, whether crystalline or amorphous, lattice periodicity and probe nucleus-complexes. Hyperfine interactions occur between a nucleus and its surrounding environment that arise from the interactions between the static magnetic and electric moments of the nucleus with the electron charge distribution in its immediate vicinity [22, 26].

2.5.1 Isomer shift

Resonance absorption occurs at zero velocity between the source and absorber if both the source and absorber are in the same environment [22]. When the local environments are different, the electron densities at the nuclei in the source and the absorber will be different. As a result, a small increase or decrease of the transition energy is required for resonance absorption to occur. This is experimentally achieved by giving source or detector a small velocity along the direction of propagation of the gamma-ray for absorption or emission experiments, respectively, and the Doppler effect due to this motion then results in an increase or decrease of the photon energy. In Emission Mössbauer experiments, the sample is a fixed source and the detector is the moving observer [22, 26]. This shift in the centroid of the resonance from zero relative velocity is known as the isomer shift. As seen in Figure 2.9,

it is observed in the Mössbauer spectrum as a shift of the absorption line and resembles the velocity at which maximum resonant absorption occurs.

The isomer shift results from the electric monopole interaction between the charge distribution of the nucleus, which is spherical in this context, and the s-electronic charge density in its immediate neighbourhood. This may not be the same in the source and absorber and, hence, causes a difference between the absorber and the source transition energies [22, 26].

The isomer shift is usually reported with respect to a standard absorber as a reference where this reference is defined to have isomer shift $\delta = 0.00\ \mathrm{mm\ s^{-1}}$. The common reference for ^{57}Fe Mössbauer spectroscopy is α-Fe at room temperature. The isomer shift only depends on the s-electron wave function of the absorber or detector, because of the s-electrons' ability to penetrate the nucleus. It may be written as

$$\delta = \alpha\{|\,\Psi\,(0)|_a^2 - C\}, \tag{2.17}$$

where $|\,\Psi\,(0)|_s^2 = constant$, is the electron probability density at the probe site and $\alpha = -0.3666\ \mathrm{mm\ s^{-1}} \cdot \mathrm{au}^3$, is the isomer shift calibration constant [22]. The isomer shift reflects the chemical bonding environment of the probe nucleus and is sensitive to the charged state of the ^{57}Fe probe nuclide.

High-spin Fe^{2+}, which has six 3d-electrons, has more shielding than high-spin Fe^{3+}, having only five 3d-electrons. The larger the shielding effect, the smaller the s-electron density at the nucleus and, consequently, a higher isomer shift. It is difficult to distinguish from only the isomer shift the valence or spin state of Fe. It is necessary to determine the quadrupole splitting and the magnetic hyperfine interaction that give further information on the possible valence state of Fe [22, 26].

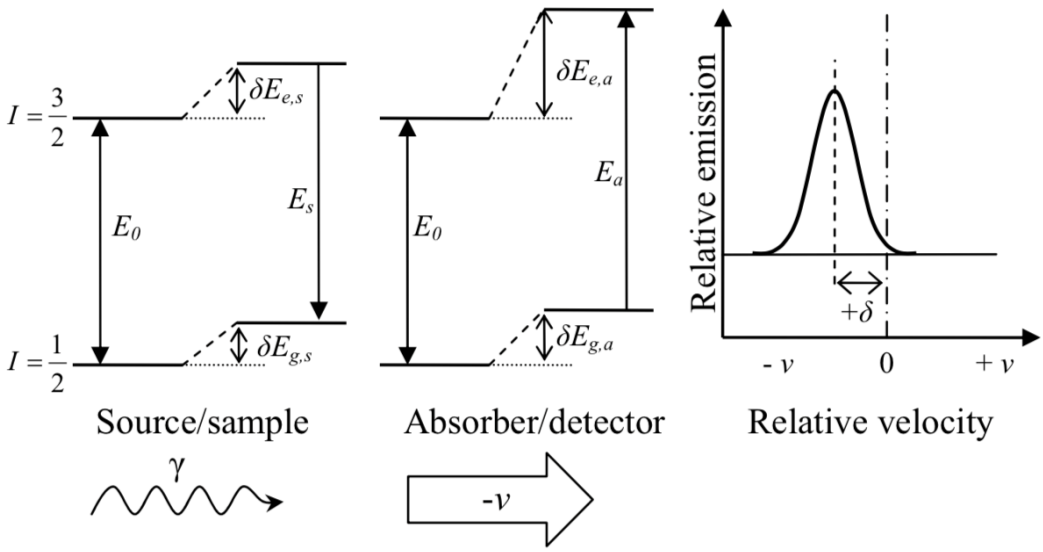

Figure 2.9: The isomer shifts and the resulting emission Mössbauer spectrum [28].

By definition of the Mössbauer velocity scale, for emission Mössbauer spectroscopy, with its fixed source and moving observer, the signs of the velocity shift and the isomer shift are opposite to that in conventional transmission Mössbauer spectroscopy.

2.5.1.1 Second order Doppler shift

The thermal motion or lattice vibrations of the nuclei result in a temperature-dependent effect which contributes to a shift in the energy and on the center shift of a Mössbauer spectrum. This phenomenon is known as the Second Order Doppler shift [22, 26]. The observed isomer shift, δ, is given by

$$\delta = \delta_{IS} + \delta_{SOD}. \tag{2.18}$$

where δ_{IS} is the true isomer shift and δ_{SOD} is a second order correction due to relativistic second order contribution to the Doppler effect. This results in a change in energy of the emitted gamma rays given by

$$\frac{\partial E}{E} = -\frac{E_\gamma}{2c^2}\langle v^2 \rangle \tag{2.19}$$

where E_γ is the energy of the gamma-ray emitted by the nucleus, c is the speed of light and $\langle v^2 \rangle$ is average velocity of the emitting nucleus. An increase in $\langle v^2 \rangle$ with increasing temperature shifts the signal towards more negative velocities [26, 38].

Following the Debye approximation as a means to describe the lattice vibrations, the shift in the isomer shift as a result of the contribution of the second order Doppler shift is given by

$$\delta_{SOD} = -\frac{3}{2}\frac{k_B\,\theta_D}{mc}\left[\frac{3}{8} + 3\left(\frac{T}{\theta_D}\right)^4 \int_0^{\frac{\theta_D}{T}} \frac{x^3}{e^x - 1}\,dx\right]. \tag{2.20}$$

2.5.2 Quadrupole splitting

A nuclear state with an angular momentum quantum number of $I > \frac{1}{2}$, has a non-spherical charge distribution, which gives rise to a quadrupole moment, Q. This nuclear quadrupole moment of the probe nucleus interacts with an inhomogeneous electric field at the nucleus, which is described by an electric field gradient, resulting in the splitting of the nuclear energy levels [22, 26]. The electric field gradient, which provides a measure of the inhomogeneity of the electric field, is described by the 3×3 tensor

$$\nabla E = -V_{jj}\frac{\partial V}{\partial x_i \partial x_j}, \tag{2.21}$$

where V is the electric potential at the probe and $i, j = x, y, z$ with respect to the axes of the electric field gradient (EFG).

A measure of the deviation of the electric field gradient from axial symmetry is given by the asymmetry parameter η which is given by

$$\eta = \frac{V_{xx} - V_{yy}}{V_{zz}}, \tag{2.22}$$

where $0 \leq \eta \leq 1$ [29].

The electric field gradient at the nucleus may result from different contributions such as the asymmetry in the lattice contribution, charges on distant ions and the valence contribution due to incompletely filled electron shells and molecular orbitals. There are two fundamental sources that contribute to the electric field gradient so that

$$V_{zz_{total}} = V_{zz_{lat}} + V_{zz_{val}}. \tag{2.23}$$

$V_{zz_{lat}}$ is the lattice contribution from the charges on the neighbouring ions or ligands surrounding the probe atom and $V_{zz_{val}}$ is the the valence electron contribution as a result of the changes in the partially filled valence orbitals of the atom [22, 26].

This interaction results in a splitting of energy levels of a nucleus that is proportional to m^2, where m is the magnetic quantum number of the level. The quadrupole interaction leads to a splitting of a nuclear transition from a single peak into two peaks. The degree of splitting of these lines is a measure of the energy difference between the sub-states and depends on the orientation and magnitude of the electric field gradient and the nuclear quadrupole moment. If a ^{57}Fe probe is located in a non-cubic environment and no magnetic interaction is present, a doublet centered at the isomer shift will be observed in the spectrum. The separation between the two peaks reflects the characteristics of the electric field at the nucleus [28]. The distance between the two resonant lines corresponds to the energy difference ΔE_Q, quantified as the quadrupole splitting, as shown in Figure 2.10. The quadrupole splitting is given by the expression

$$\Delta E_Q = \pm \frac{eQV_{zz}}{2}\left(1 + \frac{\eta^2}{3}\right)^{\frac{1}{2}}. \tag{2.24}$$

Therefore, the quadrupole splitting observed in a particular system reflects the deviation of the nuclear charge distribution from spherical symmetry of the bonding environment and the local structure in the vicinity of the atom. For ^{57}Fe in its excited state, $I = \frac{3}{2}$, where $Q \neq 0$, the electric quadrupole interaction results in a splitting of the excited state into two double degenerate energy levels due to $\pm\, m_l$. The ground state, $I = \frac{1}{2}$, where $Q = 0$, does not split but is a double degenerate level. The degeneracy of the energy levels can only be altered by an external magnetic field. For the simplest case, when the EFG is axial such that $V_{xx} = V_{yy}$ and $\eta = 0$, the quadrupole splitting can be written as

$$\Delta E_Q = \frac{eQV_{zz}}{2} \tag{2.25}$$

where e is the electronic charge and V_{zz} is the maximum value of the electric field gradient.

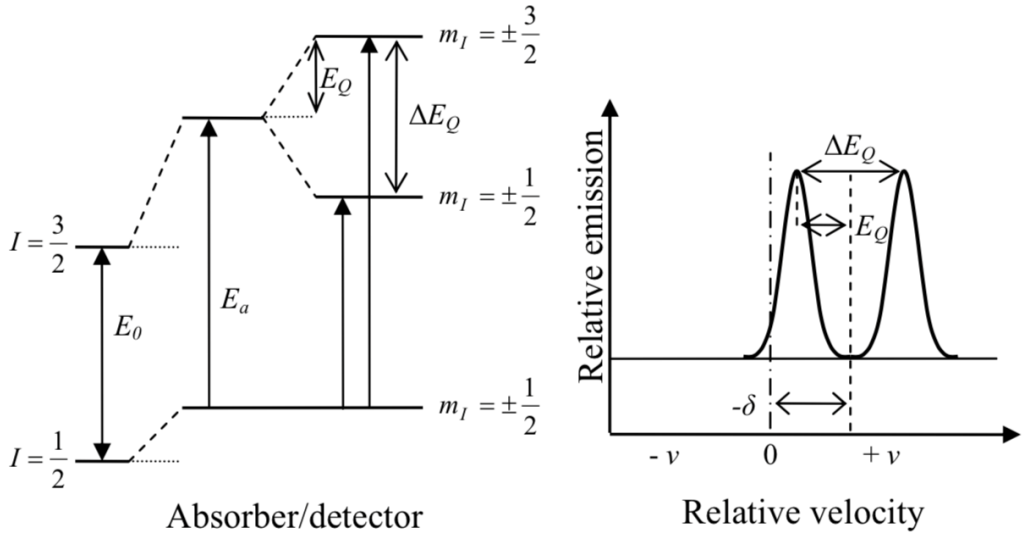

Figure 2.10: The quadrupole splitting and the resulting emission Mössbauer spectrum [28].

In Mössbauer spectroscopy the quadrupole splitting, ΔE_Q, is given in units of the drive velocity, $\mathrm{mm\ s^{-1}}$. In general, the temperature dependence of the quadrupole splitting can be used to distinguish between the spin states of the Fe, although this also depends on the crystal symmetry of the probe site [22, 26, 39].

The quadrupole splitting decreases with increasing temperature due to the temperature dependence of the electric field gradient generated by the surrounding lattice and valence electrons, with the assumption that the valence contribution is not negligible. However, for Fe^{3+}, the quadrupole splitting is not affected by removing the orbital degeneracy, hence, it is temperature independent [26, 39].

2.5.3 Magnetic dipole interaction

When a nucleus has a spin $I > 0$, it has a magnetic dipole moment, μ, which interacts with any surrounding magnetic field, B_{hf}. The energy of this interaction is given by

field direction which splits energy levels with nuclear momentum I into $(2I + 1)$ equally spaced energy states as shown in Figure 2.11. The energy of this interaction is given by

$$E = -\mu \cdot B_{hf} = -\, g_n\, \mu_N\, I \cdot B_{hf} \qquad (2.26)$$

which may be written in the form

$$E_m = -\, g_n \frac{e\hbar}{2M_p c}\, B_{hf}\, m_l. \tag{2.27}$$

where $e, \hbar$ and c are charge of the electron, reduced Planck's constant and speed of light in vacuum, respectively, g_n is the nuclear g-factor, m the magnetic quantum number, μ_N the nuclear magneton and M_p the mass of a proton. This interaction, known as the nuclear Zeeman effect or magnetic dipole interaction, results in a precession of the dipole moment about the field direction and splits an energy level with nuclear spin I into $(2I + 1)$ equally spaced energy states, as shown in Figure 2.11. For ^{57}Fe, there exists nuclear magnetic dipole moments for both the ground state and the first excited state. Hence, in a magnetic field B_{hf}, the ground state with $I = \frac{1}{2}$ splits into two sub-states with m = +1/2 and -1/2, while the excited state with $I = \frac{3}{2}$ splits into four sub-states (m= +3/2, +1/2, -1/2 and – 3/2) [29].

The selection rules for the magnetic dipole transition $(\Delta\, m_l = 0, \pm 1)$ permit six possible gamma transitions between the sub-levels. As a result, for ^{57}Fe, the spectrum splits into a sextet due to the nuclear Zeeman effect. The magnitude of nuclear Zeeman splitting is usually measured as the distance between the outermost of these six peaks. A sextet component in the ^{57}Fe Mössbauer spectrum is not only observed due to ordered magnetism - it can also originate from paramagnetism as a result of certain instances of slow relaxation [22, 26, 39].

The nuclear Zeeman splitting is of interest in Mössbauer spectroscopy for iron-containing compounds which are either ferromagnetic or anti-ferromagnetic resulting in strong internal magnetic fields [29]. The spectral line splitting is directly proportional to the magnetic field at the nucleus. The linewidths of the resulting spectra are equal, although their intensities are different. An increase in temperature reduces the magnetic hyperfine field of the spectrum due to thermal vibrations of the spins and this reduces the nuclear Zeeman splitting. From the spectra, the type of magnetic ordering in a material, the nature of the magnetic interaction as well as the size of magnetic moment on the atoms can be determined [22, 26, 39].

2.5.4 Combined magnetic and quadrupole interactions

Often both quadrupole and magnetic interactions are present, and this results in an asymmetric sextet seen in the Mössbauer spectrum [22, 26]. The quantization axes of the quadrupole interaction and the magnetic hyperfine field interaction are not necessarily the same. However, the quadrupole interaction is usually much smaller than the magnetic hyperfine field interaction and can be treated as a perturbation on the magnetic effect. In the

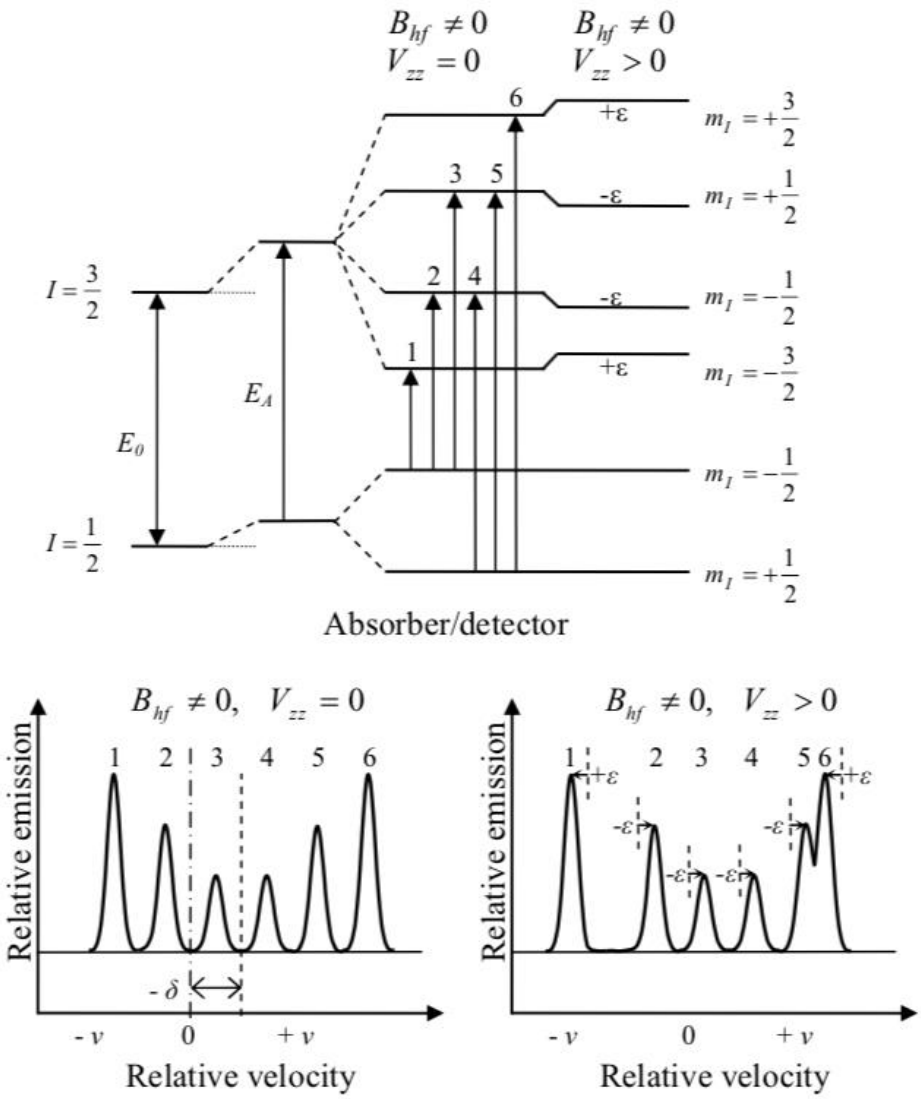

Figure 2.11.: The energy level shifts and the resulting Mössbauer spectra for magnetic dipole interaction in the absence and presence of an electric field gradient [28].

case of axial symmetry ($\eta = 0$) the perturbation can be described with the angle ω and the energy levels shift given by

$$E_{Q,m} = -\, g_n\, \mu_N\, B_{hf}\, m_l + (-1)^{|\, m_l| + \frac{1}{2}}\, \frac{eQV_{zz}}{8}\, (3cos^2\omega - 1) \qquad (2.28)$$

where, ω is the angle between the principal axis of the electric field gradient tensor and the hyperfine field and the last term gives the quadrupole shift ε. For $V_{zz} > 0$, as seen in Figure 2.11, the energy levels with $I = \frac{3}{2}$ and $m_l = \pm\frac{3}{2}$ are shifted $+\varepsilon$ and the states with $m_l = \pm\frac{1}{2}$ are shifted $-\varepsilon$ in energy [29].

3 EXPERIMENTAL DETAILS

This chapter comprises a description of the sample synthesis, the experimental set-ups and techniques applied as well as details on emission Mössbauer measurements after implantation of radioactive ^{57}Mn ions into host samples conducted at the ISOLDE facility at CERN, Switzerland. The last part of this chapter highlights the software program used for data analysis.

3.1 Sample description and preparation

Emission Mössbauer data were collected on three samples – a 94 nm thick Ba:BFO film, a 300 nm thick Ba:BFO film and an undoped BFO sample. The undoped BFO sample was synthesized at the University Duisburg-Essen by Marianela Escolar. First, a stoichiometric mixture of Bismuth oxide (Bi_2O_3) and Iron oxide (Fe_2O_3) powders were calcined for three hours at 820 °C. Thereafter, the calcined powder was pressed into pellets and sintered for six hours at again 820 °C in air. The lattice parameters of the BFO sample are: $a = b = 5.576$ Å, $c = 13.862$ Å and cell volume V = 373.29 Å^3.

Ba-doping of the samples was conducted by Sven Becker and Gerhard Jakob at the Institute of Physics, Johannes Gutenberg University - Mainz, Germany. Ba substituted BiFeO3 (Ba:BFO) samples with a Ba content of 15% were prepared by pulsed laser deposition from a target with 20% Bismuth excess to compensate loss during deposition. The deposition chamber had a base pressure of 4×10^{-8} mbar. As substrates, commercially available (001) oriented $SrTiO_3$ (STO) single crystals were used after standard buffered HF treatment [30]. The substrate temperature during deposition was 475 °C measured with a pyrometer (emission factor ε = 0.85) at the surface of the inconel substrate holder. The oxygen pressure was 0.1 mbar generated by a 99.95% pure oxygen flow of 10 SCCM and a partially opened gate valve between deposition chamber and turbo pump. The laser profile is imaged onto a 0.1 cm^2 area on the target, which results in an estimated energy density of 640 mJ cm^{-2}. The laser had a wavelength of 248 nm (Compex Pro205, KrF) and was used with a repetition rate of 5 Hz. The substrate to target distance was 5.5 cm. These parameters result in a film growth rate of 1 Å/s. For small thicknesses the growth mode is layer-by-layer. Figure 3.1 shows the surface

topography of a Ba:BFO(300 nm)/STO sample measured by atomic force microscopy (AFM). The material seems to reproduce the unit cell steps of the STO substrate originating from a miscut. Small islands of Ba:BFO of unit cell height form on the surface before merging into a continuous layer. X-ray reflectivity confirms a low mean roughness of the samples (not shown).

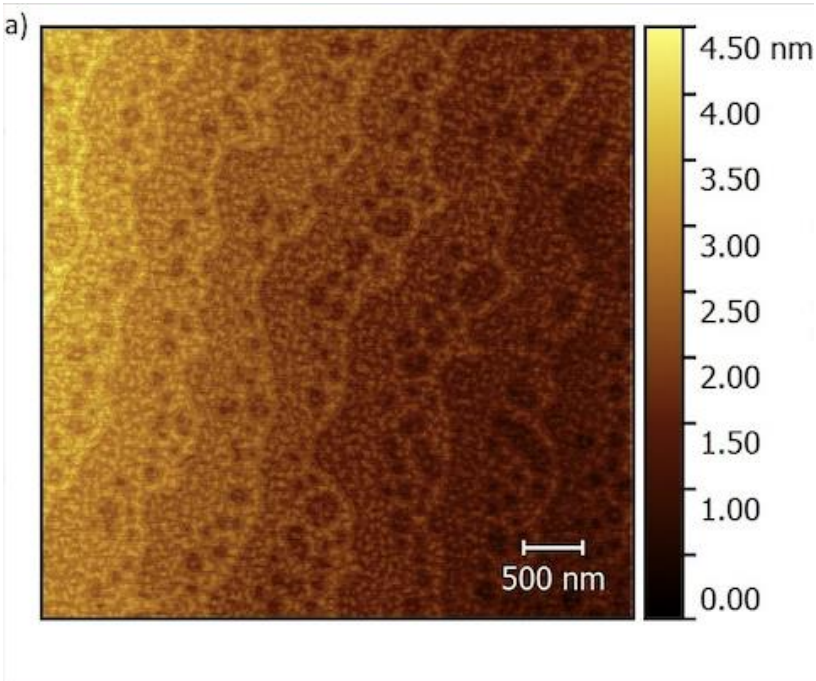

Figure 3.1: Atomic force microscopy image of surface topography of a Ba:BFO(300 nm)/STO sample measured by atomic force microscopy (AFM).

The structural properties of the samples were characterized by X-ray diffraction. The 2Θ/ω scan in Figure 3.2 shows that Ba:BFO grows single phase with an out-of-plane lattice constant of 4.2 Å. Omega scans of the (001) Ba:BFO reflex (not shown) reveal a narrow rocking curve of 0.03° FWHM indicating a well oriented crystal. From the reciprocal space map around the (103) STO substrate peak in Figure 3.3, it was concluded that Ba:BFO grows fully strained box-on-box on STO in a tetragonal phase with a c/a ratio of 1.07 which coincides with the results from Mix and Kim [16, 41] for pure $BiFeO_3$ (BFO) on STO.

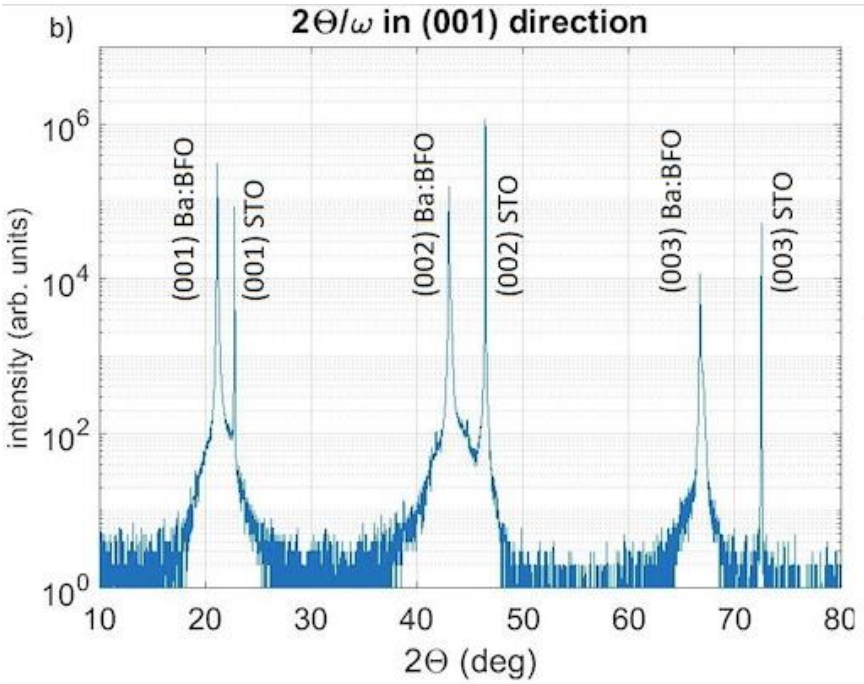

Figure 3.2: Omega scans of a Ba:BFO(300 nm)/STO sample.

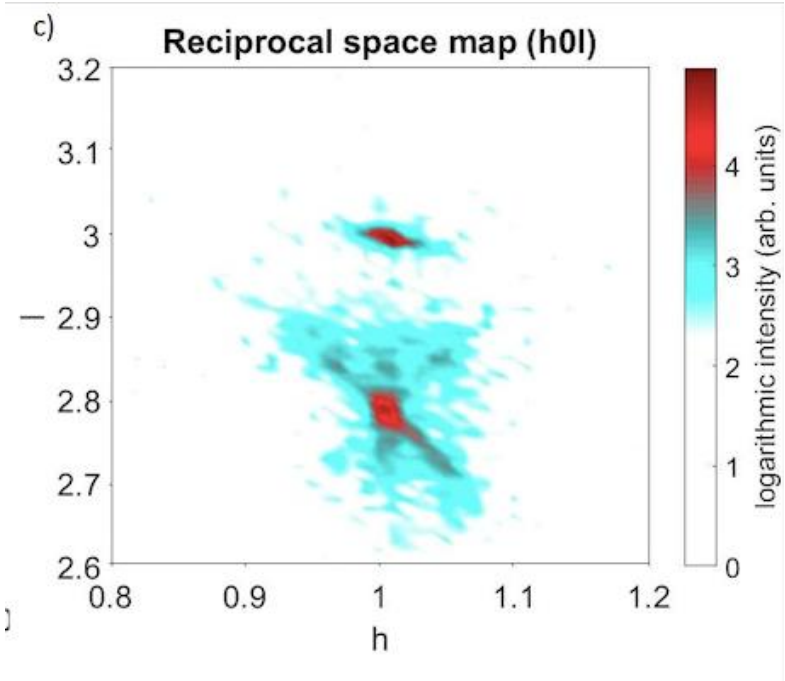

Figure 3.3: A reciprocal space map of a Ba:BFO(300 nm)/STO sample.

3.2 Emission Mössbauer spectroscopy at the ISOLDE facility

The ISOLDE facility is an on-line isotope separator facility dedicated to the production of a variety of radioactive ion beams for a variety of experiments [25]. This facility is located at the Proton-Synchrotron Booster (PSB) accelerator complex at CERN and is operated by the ISOLDE Collaboration. The radioactive nuclides are produced in reactions of high-energy (1.4 GeV)

protons from the PSB accelerator in thick targets via fission or fragmentation reactions and are delivered to the ISOLDE target area via an underground transfer line [27].

Targets are placed in the external proton beam of the PSB which has energy of $1.0\ \mathrm{GeV}$ or $1.4\ \mathrm{GeV}$. The target used at the on-line isotope separator is a fast liberator of radioactive nuclei [27]. The target material is kept at an elevated temperature between 700 °C and 1400 °C so that the produced radioactive atoms diffuse out of the target into different dedicated ion sources. Ionization can take place in hot plasma, on a hot surface or by laser excitation. The combination of the target and ion source produces an ion beam that contains only isotopes from one element [27]. An electric field accelerates ions to an energy of up to 60 keV which are then mass separated and steered to the experiments [24]. The ISOLDE facility has two isotope separators - the General Purpose Separator (GPS) and the High Resolution Separator (HRS). The GPS is designed to allow three beams (central mass, low mass and high mass) to be selected and transported into different beam lines in the experimental hall [27].

The radioactive ions are employed for nuclear investigative techniques such as Perturbed Angular Correlations (PAC), Mössbauer Spectroscopy (MS) and Emission Channeling (EC). Applications of these techniques allow the investigation of radiation damage, lattice sites of dopants, site selective doping of semiconductors, donor-acceptor interactions in semiconductors, diffusion studies, and the investigation of surfaces and interfaces [25].

The exclusive feature of Mössbauer spectroscopy is its ability to probe the local environment at an atomic scale and in turn provide information on the lattice sites, symmetry, charge states and magnetic interactions of the Mössbauer nuclide [24]. The Mössbauer experimental setup at CERN is connected to the on-line mass separator, hence, the term ‘on-line Mössbauer spectroscopy’. The usage of radioactive isotope beams for on-line Mössbauer spectroscopy has proved to be a powerful method to obtain the properties of an absorbing and emitting nuclei [24]. The on-line Mössbauer arrangement using a radioactive pre-cursor has the advantage that both ion implantation and probing of the lattice can be performed at the same time.

^{57}Fe emission Mössbauer spectroscopy utilizes the radioactive precursor isotope $^{57}Mn^{+}$ ($t_{1/2}$ = 85.4 s) produced at the ISOLDE, CERN as implantation probe atoms [24]. This isotope decays to ^{57}Fe Mössbauer state that can be used to study the magnetic properties, lattice locations and charge states of materials under study. In Figure 3.4, the location of the Mössbauer experimental set-up within ISOLDE is illustrated [28].

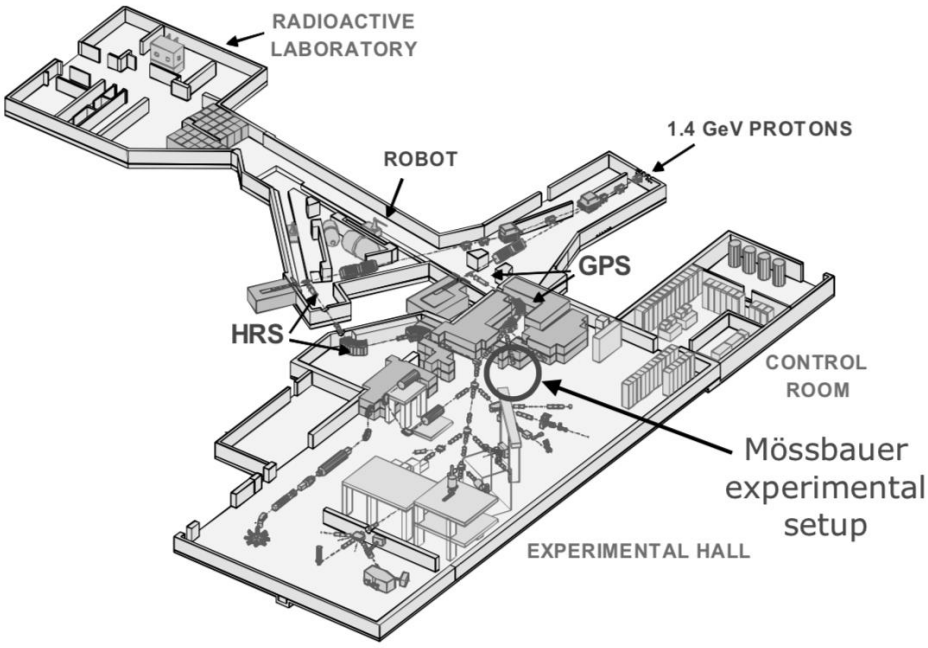

Figure 3.4: The ISOLDE facility at CERN, Geneva, Switzerland [28].

3.2.1 Beam production

The ^{57}Mn isotope is not a Mössbauer isotope. It decays via β^{-} to ^{57}Fe, the most widely used isotope for Mössbauer spectroscopy ^{57}Fe [25]. The ^{57}Mn nucleus decay has a half-life of 90 s that is advantageous for on-line measurements, as the implanted probes will not have enough time to out-diffuse and high statistics ^{57}Fe Mössbauer spectra can be collected within 5 – 10 min. This on-line method of populating the 14.4 keV ^{57}Fe Mössbauer state ($t_{1/2}$ = 98.3 ns) which has a narrow natural line-width (~0.097 mm s^{-1}) allows the study of truly dilute samples with local concentration of the implanted species below 10^{-3} at. % [25]. A few important measured properties of this state are α_T, the ratio of transitions by conversion electrons to transitions by photons, which is equal to ~8.21 and means that approx. 8 out of every 9 transitions take place by conversion electron emission, μ the magnetic moment (= 0.09 μ_N)

and eQ, the electric quadrupole moment (= +0.21 b) [32]. The natural line width Γ is 4.665(7) x 10^{-9} eV, which for ^{57}Fe gives the energy conversion of 1 mm s^{-1} = 4.80766(3) x 10^{-8} eV [32].

A negative impact of using ^{57}Mn as a precursor to populate the ^{57}Fe Mössbauer state is that because of the low concentrations required to yield a spectrum with good statistics, no complimentary measurements can be made except for pre-characterization of a sample. In post-implanted samples with low concentration of ~10^{-3} at. % Mn/Fe ions, conventional magnetization measurements will be futile as the magnetization effects will be undetectable. In Figure 3.5, the decay scheme of ^{57}Fe from different parent nuclei is illustrated [32].

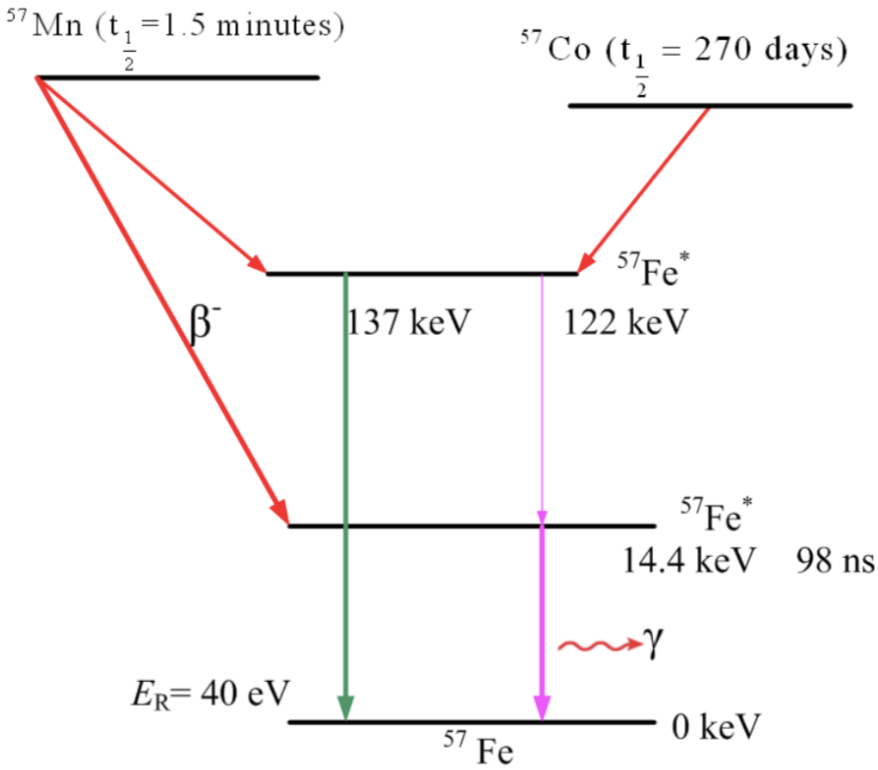

Figure 3.5: Decay scheme of ^{57}Fe from parent nuclei ^{57}Co and ^{57}Mn [32].

Radioactive $^{57}Mn^{+}$ beams are produced at the ISOLDE Facility, using 1.4 GeV proton-induced nuclear fission in a uranium carbide (UC_2) target. The fission fragment atoms diffuse to the surface where they are desorbed and are ionized with elemental selective multi-photon laser ionization and at the same time ^{57}Fe contaminants of up to 10^{10} ions/s in the beam are removed [24]. The singly charged ions are then accelerated to energies between 40 - 60 keV

before they are mass separated by a magnetic field to produce pure radioactive $^{57}Mn^{+}$ ion beams of ~2×10^{8} $^{57}Mn^{+}$/s which are then directed to the implantation chamber. 40 keV is at the lower edge of acceptable implantation energy, as a larger fraction of the implanted ions will end up too close to the sample surface resulting in surface effects [28]. A beam spot area of 0.3 cm^2 corresponds to a flux of ~6.2×10^{8} $^{57}Mn^{*}/(cm^2\ s)$ [24]. In the ^{57}Mn to ^{57}Fe decay, the recoil energy imparted to the ^{57}Fe is on average 40 eV, which results in an appreciable fraction of the ^{57}Fe replacing the Fe in the BFO and BBFO. Hence, these are favorable probes of the magnetism in the host material. The beam production at ISOLDE described by the ISOL-principle is illustrated in Fig. 3.6 [24].

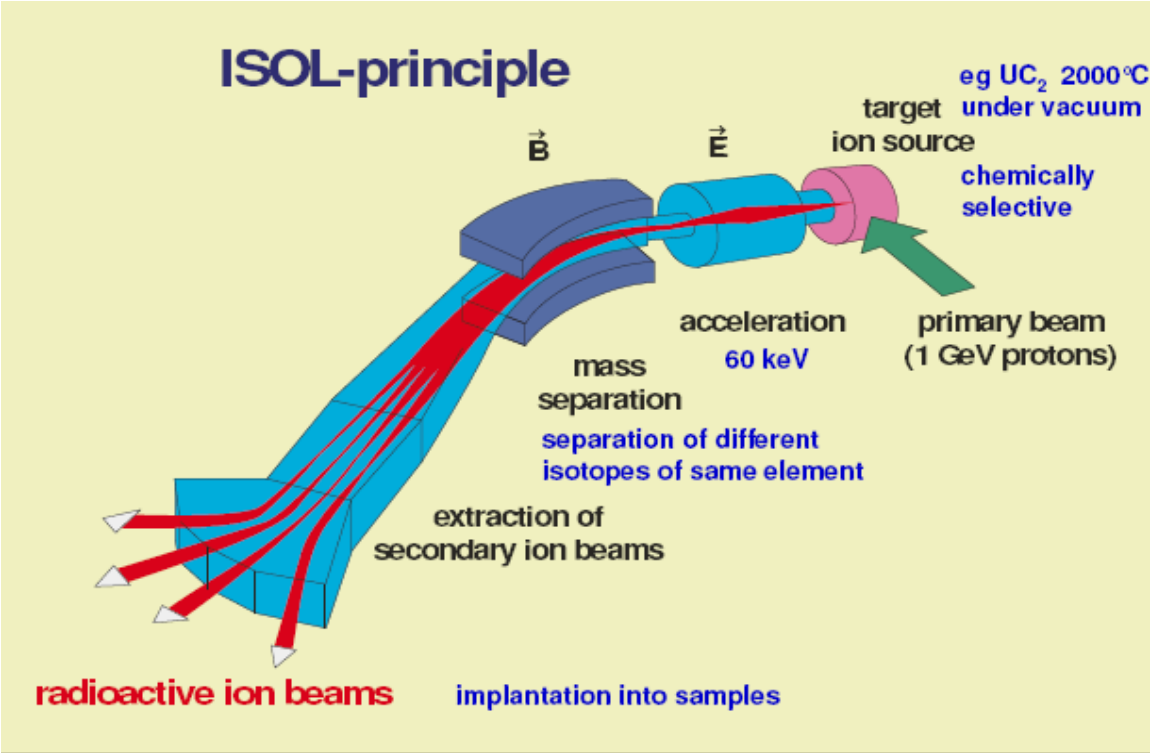

Figure 3.6: Beam production at ISOLDE [24].

Figure 3.7, presents the implantation profile of ^{57}Mn into bismuth ferrite which was simulated using "The Stopping and Range of Ions in Matter" or "SRIM" software developed by Ziegler *et al.* [25]. The average implantation range is estimated to be 19.8 nm with a straggle equal to 10.8 nm. These values are well below the 98 nm thickness of the BFO film.

A density of 8.38 $g.cm^3$ for BFO corresponds to an atomic density of 8.07 x 10^{22} $atoms/cm^3$. The maximum peak concentration of the implanted Mn ions is equal to the maximum total

fluence (5 x 10^{12} ions/cm^2) multiplied by the peak of the implantation profile where, the number of ions is the fluence multiplied by 3.4 x 10^5 counts. This gives the peak Mn concentration of 17.0 x 10^{17}/cm^3, which corresponds to an atomic density of 2.1 x 10^{-3} at. %. In Figure 3.8, a plot of the Bi, Fe and O recoils produced in bismuth ferrite by 45 keV Mn ions, as estimated by the TRIM software [33], is presented.

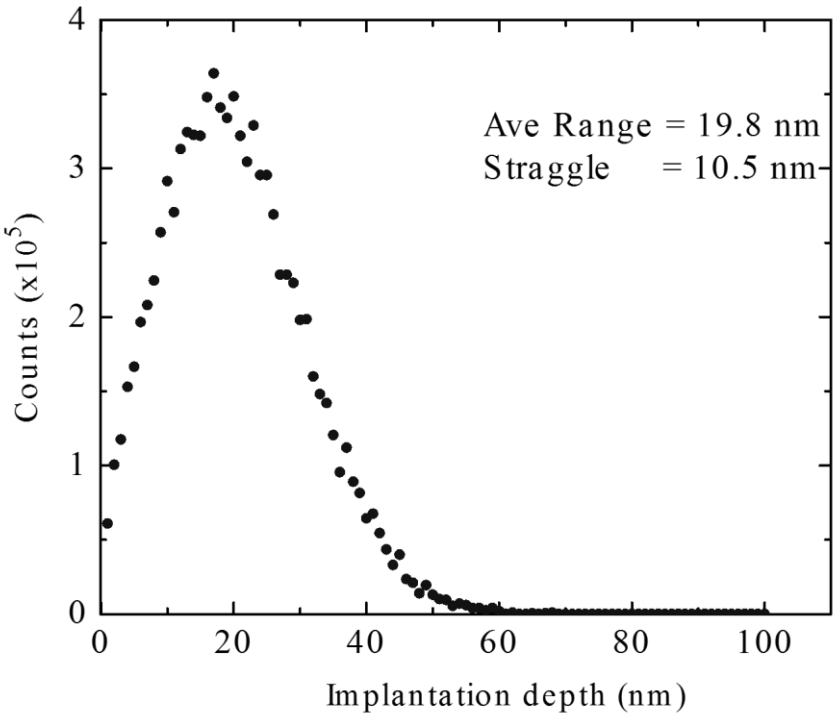

Figure 3.7: The implantation profile of 45 keV ^{57}Mn *implanted in* BFO *at a 30° angle.*

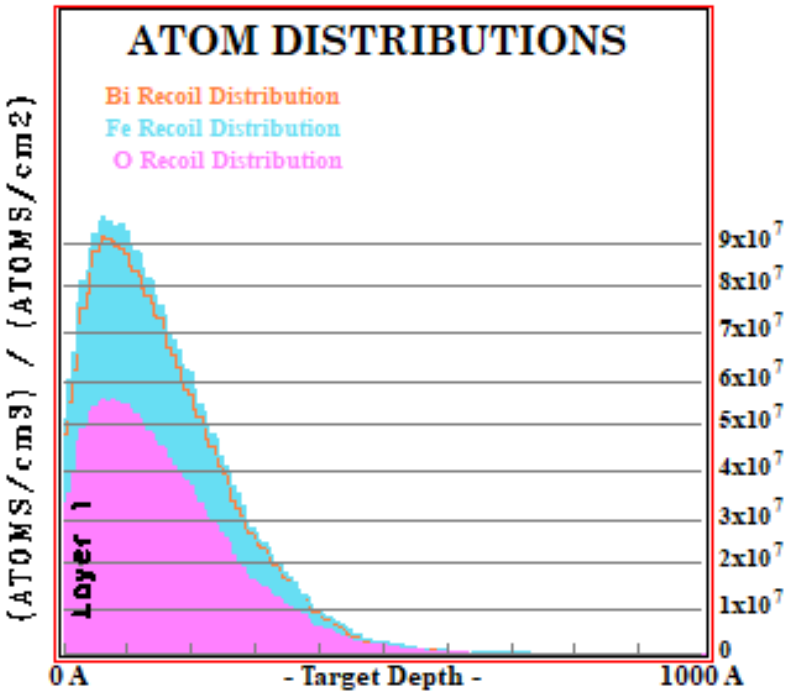

Figure 4.8: TRIM estimates of the Bi, Fe and O recoil profiles in Mn implanted $BiFeO_3$.

3.2.2 Experimental set-up

The main components of the setup consist of an implantation chamber, Mössbauer drive unit, resonance detector, sample holder and the necessary electronics as seen in Figure 3.9 [24].

The high vacuum implantation chamber is connected by soft bellows to the $^{57}Mn^{+}$ beamline system and is pumped to 10^{-6} mbar. A liquid N_2 cryostat system is connected to the implantation chamber for low temperature (77 - 300 K) measurements using a single-position sample holder. A four-position sample holder is used for high temperature measurements (300 – 700 K) which allows for a series of measurements on four different samples without having to open the system to mount new samples and to pump down to good vacuum as often as required [24].

As a first step, two sample holder positions were allocated, one without a sample for beam alignment of the implantation chamber with the beam and current optimization, the other with an α-Fe foil for calibration of the drive system. First, a beam of stable ions was directed through the first empty sample position towards the Faraday cup, which is designed to collect charged particles, to optimize the beam current. This was achieved by varying the beam

steering parameters on the ISOLDE console in the control room. Then a beam of ^{57}Mn ions was directed onto the α-Fe absorber and the resulting α-Fe spectrum, with its well established positions of spectral components in terms of the velocity of the drive unit, was collected. This spectrum was used for calibration of the drive velocity as well as to set the reference zero position for all hyperfine parameters determined from the measurements [24, 28-29].

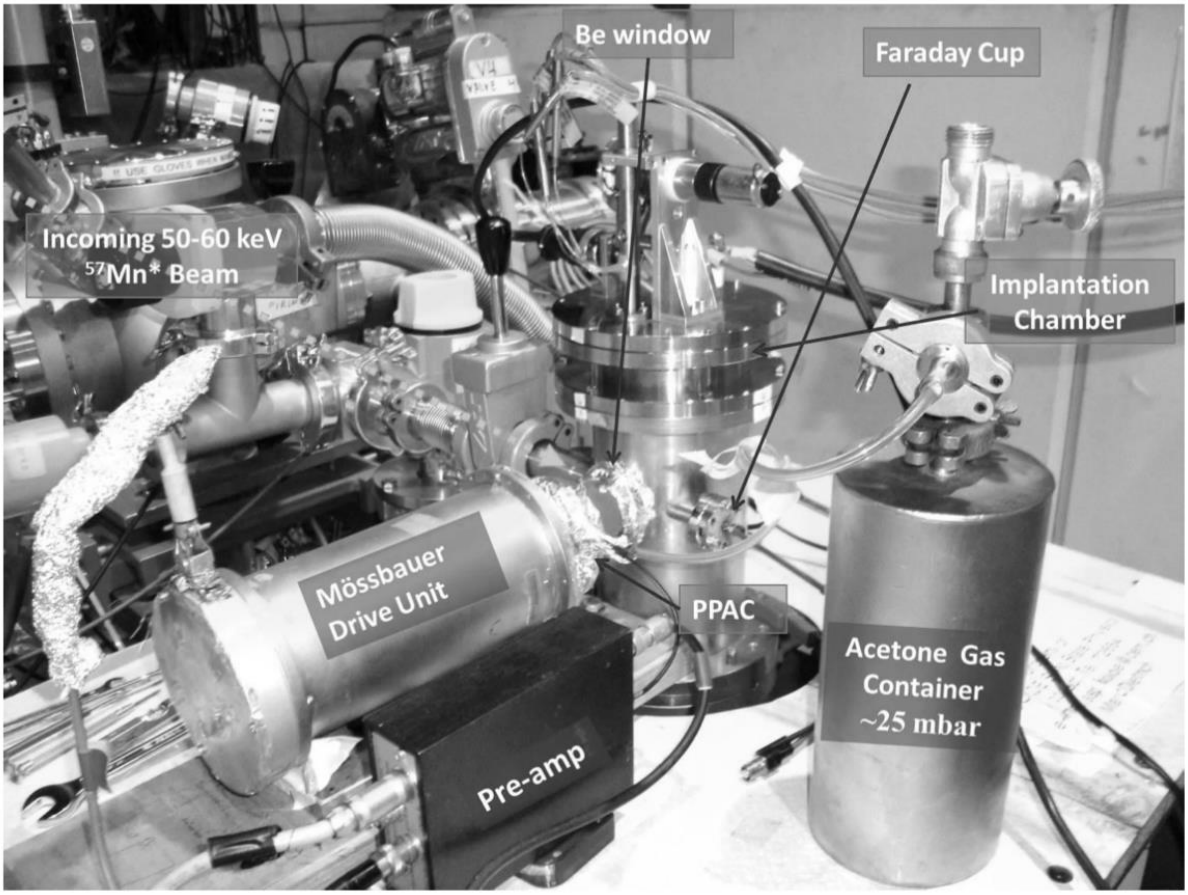

Figure 3.9: Emission Mössbauer spectroscopy set-up at ISOLDE, CERN [24].

An Osram halogen photo-optic lamp (15 V, 150 W) was fixed in the implantation chamber to provide thermal heating of the sample with a temperature range up to approximately 800 K. A 1 mm thick beryllium foil, which has low absorption probability for the ^{57}Fe 14.4 keV gamma-rays was used as window on the UHV implantation chamber facing the detector.

In emission Mössbauer spectroscopy, the sample is the source of gamma-radiation and a single line absorber material is utilized in the detector. A parallel-plate avalanche counter (PPAC) detector was mounted on the Mössbauer drive unit outside the implantation

chamber, providing the velocity drive and the Doppler shift in energy of the emitted gamma-radiation required to record Mössbauer spectra [24]. The detector was moved using triangular drive signal (linear velocity scale) as a function of time [25]. A PPAC detector consists of two conductive plates (cathode and anode) mounted in parallel to each other with a small separation of 3 mm and filled acetone gas. The cathode was made of a stainless-steel foil enriched in ^{57}Fe while the anode was made of graphite. A bias voltage was applied to create a homogeneous electric field between the plates [24] which accelerates conversion electrons from the ^{57}Fe decay towards the anode. The beam current of $^{57}Mn^{+}$ was low compared to stable beams, hence, the use of PPAC detectors in data acquisition. These were fast and insensitive to gamma- or X-ray background radiation, i.e. the signal to background ratio is high and they have a relatively high time resolution in the order of nanoseconds (10^{-9} s). Therefore, high count rates can be tolerated [24].

The PPAC was connected in series to a high voltage supply and pre-amplifier. The pulses from the PPAC were pre-amplified and fed to the main amplifier which then directed amplified DC voltage pulses to a single channel analyzer (SCA) in which discriminator levels were set to eliminate non-resonant background radiation and detector and pre-amplifier noise. Thereafter, the filtered pulses were sent to the Multi- Channel Analyzer (MCA) unit operating in multichannel scaling mode (MCS) in which the start time of the sweep and the dwell time in each channel was synchronized with the Mössbauer Drive Unit (MDU) by STA (start) and CHA (Channel Advance) outputs from the MDU. A digital function generator (DFG) allows the use of a sinusoidal or saw tooth (linear drive) drive function [24]. The MCA card was installed in a computer used for the accumulation of the data and visualization of the spectra in which the counts were accumulated in channels, either 512 or 1024. A schematic diagram of the experimental set-up is illustrated in Figure 3.10 [24].

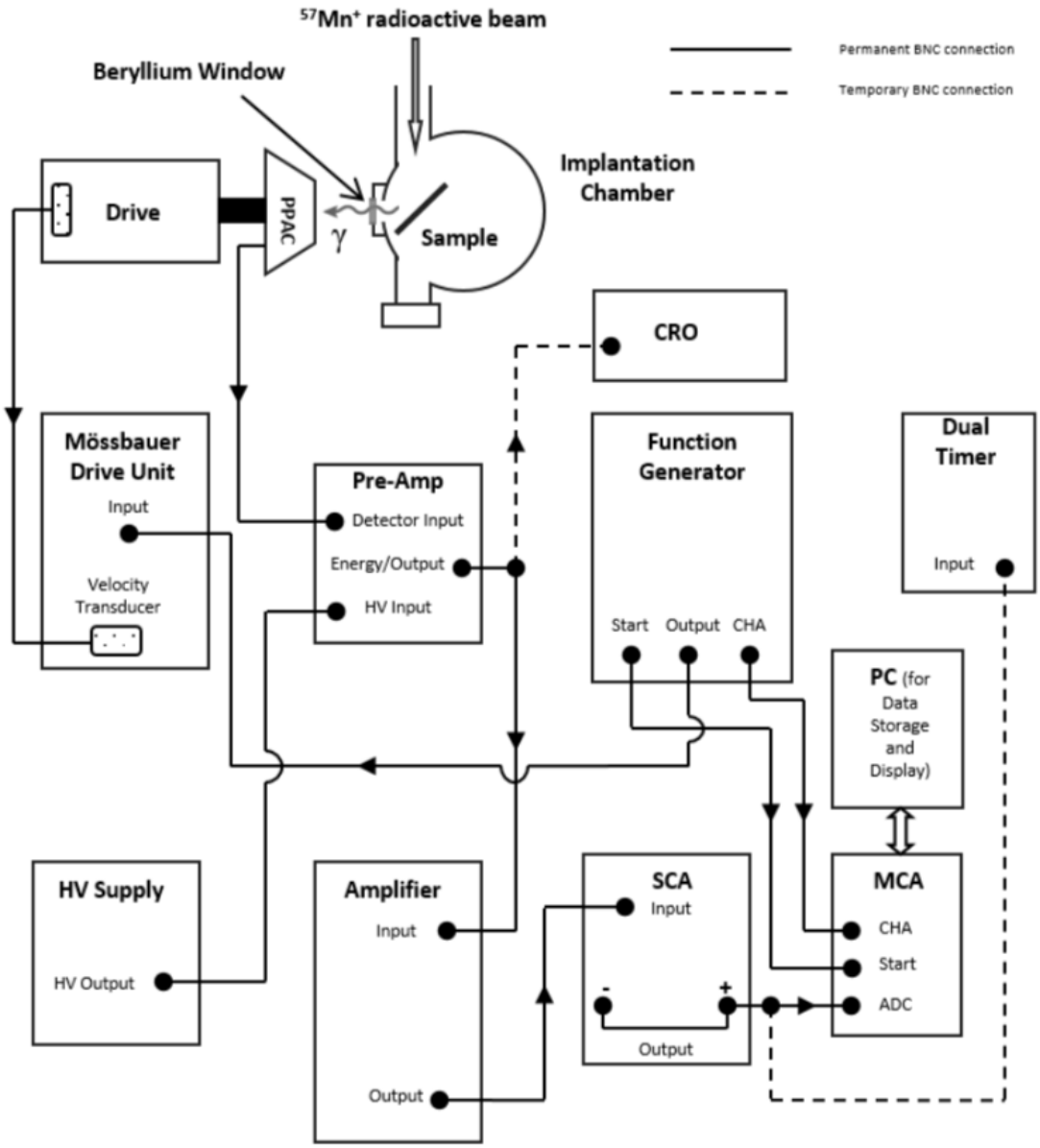

Figure 3.10: Schematic diagram of the experimental set-up, including electronics, at ISOLDE [24].

3.3 eMS measurements

Following the set-up described in section 3.2.2., the sample was mounted on a four-position sample holder and inserted into the implantation chamber and placed at an angle of 30° with respect to the Mn beam axis. Following implantation of $^{57}Mn^{+}$ ions of 45 - 50 keV into the sample, low temperature measurements, as low as 180 K, and measurements during an annealing sequence from 300 K to 700 K were then completed. The samples were heated by

irradiation from the halogen photo-optic lamp from the rear. Mössbauer spectra were recorded using the resonance detector (PPAC) described in section 3.2.2. The measurements were conducted on a wide velocity scale of ±12 mm s^{-1}. Measurements times of 8-12 minutes were sufficient to give spectra with good statistics.

The drive velocity was calibrated using an α-Fe absorber due to its well-defined magnetic sextet of absorption lines which also provided the reference point for the isomer shifts of the spectral components. The first step of the calibration was to fold the spectrum of number of counts dependent on the channel number which results in the relative emission spectrum as a function of velocity. Thereafter, estimated values from previous literature of the relevant hyperfine parameters were input as starting values and the spectra was fitted accordingly with the aid of the programme VINDA developed by Dr H.P. Gunnlaugsson [34]. The Vinda programme operates within Microsoft Excel, where all commands are contained in a toolbar that runs Visual Basic for Applications macros. This program enables simultaneous analysis of the spectra for an entire temperature range and also does an error analysis [25].

4 RESULTS AND DISCUSSION

This chapter focuses on the analysis and interpretation of data obtained from online emission Mössbauer Spectroscopy (eMS) following ^{57}Mn implantation into BBFO and BFO samples. The results presented here were obtained in eMS measurements performed as a function of temperature. The Mössbauer hyperfine parameters were determined from analysis procedures using the Mössbauer analysis code VINDA [34].

4.1 Analysis of data and results of BBFO sample of thickness 94 nm

4.1.1 Mössbauer spectra

Figure 4.1 displays the Mössbauer spectra obtained for the Ba substituted $BiFeO_3$ (BBFO) thin film of thickness 94 nm. A visual inspection of the series of spectra shows that the magnitude of the main magnetic sextet decreases with an increase in temperature. Earlier EMS measurements on ZnO and a range of metal oxides yielded spectra with magnetic sextets which showed no decrease in the hyperfine field strength [24]. These data were interpreted on the basis of slow paramagnetic spin relaxation attributed to the relatively long spin-lattice relaxation time between the spin of the probe nucleus (^{57}Fe) and the host lattice. The present results argue against the applicability of such an interpretation to the magnetic phenomena observed in the present study on the Ba doped BFO samples.

The spectra were fitted with the following spectral components - a symmetric sextet, B_1, two quadrupole split doublets, D1 and D2, modeled by Voigt line shapes, one of which is asymmetric and the other symmetric, and a magnetic distribution, $B_{distribution}$ which is a combination of sextets that are attributed to Fe in implantation induced defects.

The room temperature (RT) spectrum is characterized by two sextets and a symmetric doublet as seen in Figure 4.1, whereas at higher temperatures the spectrum is dominated by the asymmetric doublet. In Figure 4.2, the Mössbauer spectra of the BBFO (94 nm) sample observed at the temperatures indicated are presented on a smaller vertical scale so that the fitting of the main magnetic component may be studied in greater detail.

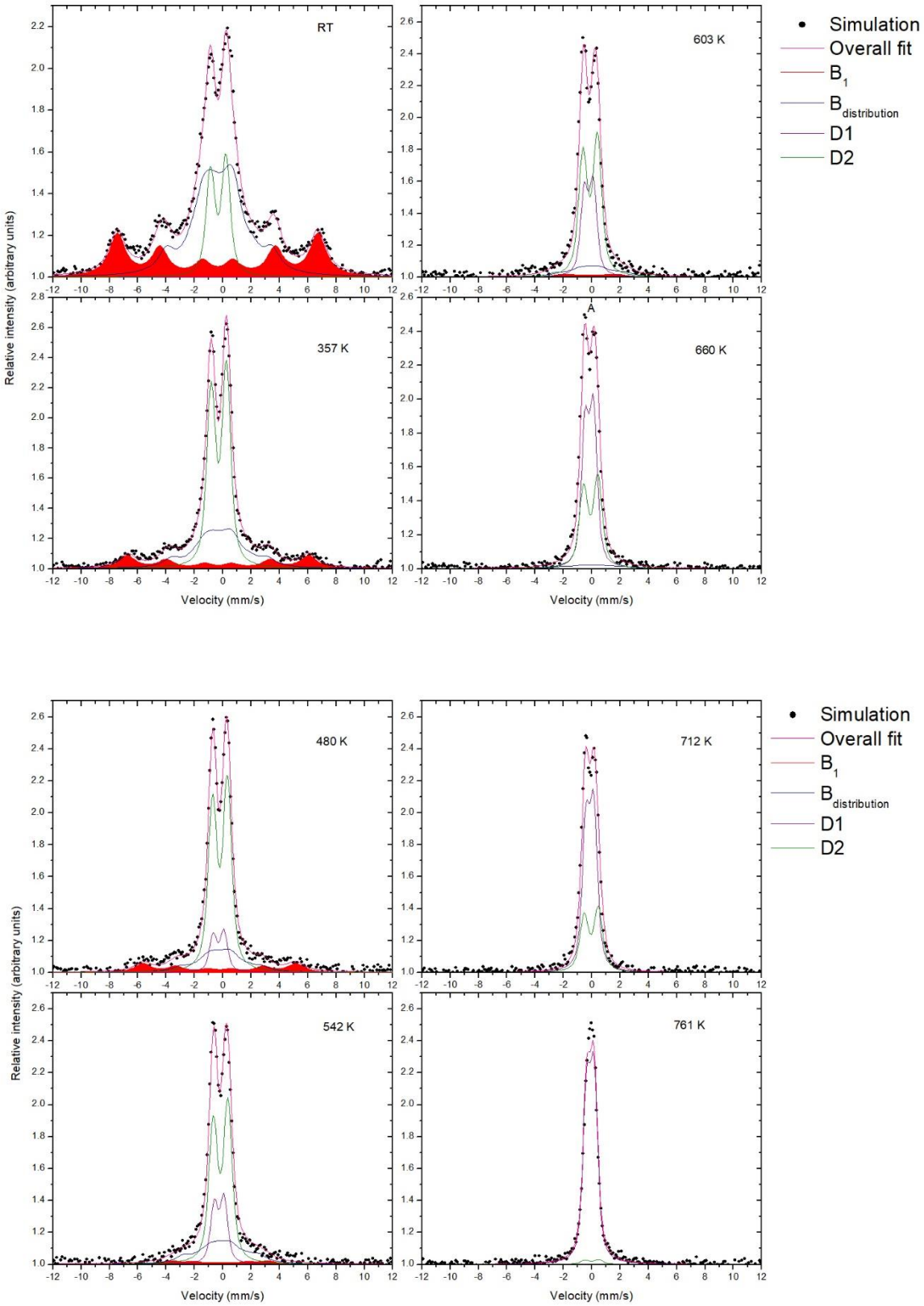

Figure 5.1: Mössbauer spectra of the BBFO (94 nm*) sample observed at the temperatures indicated.*

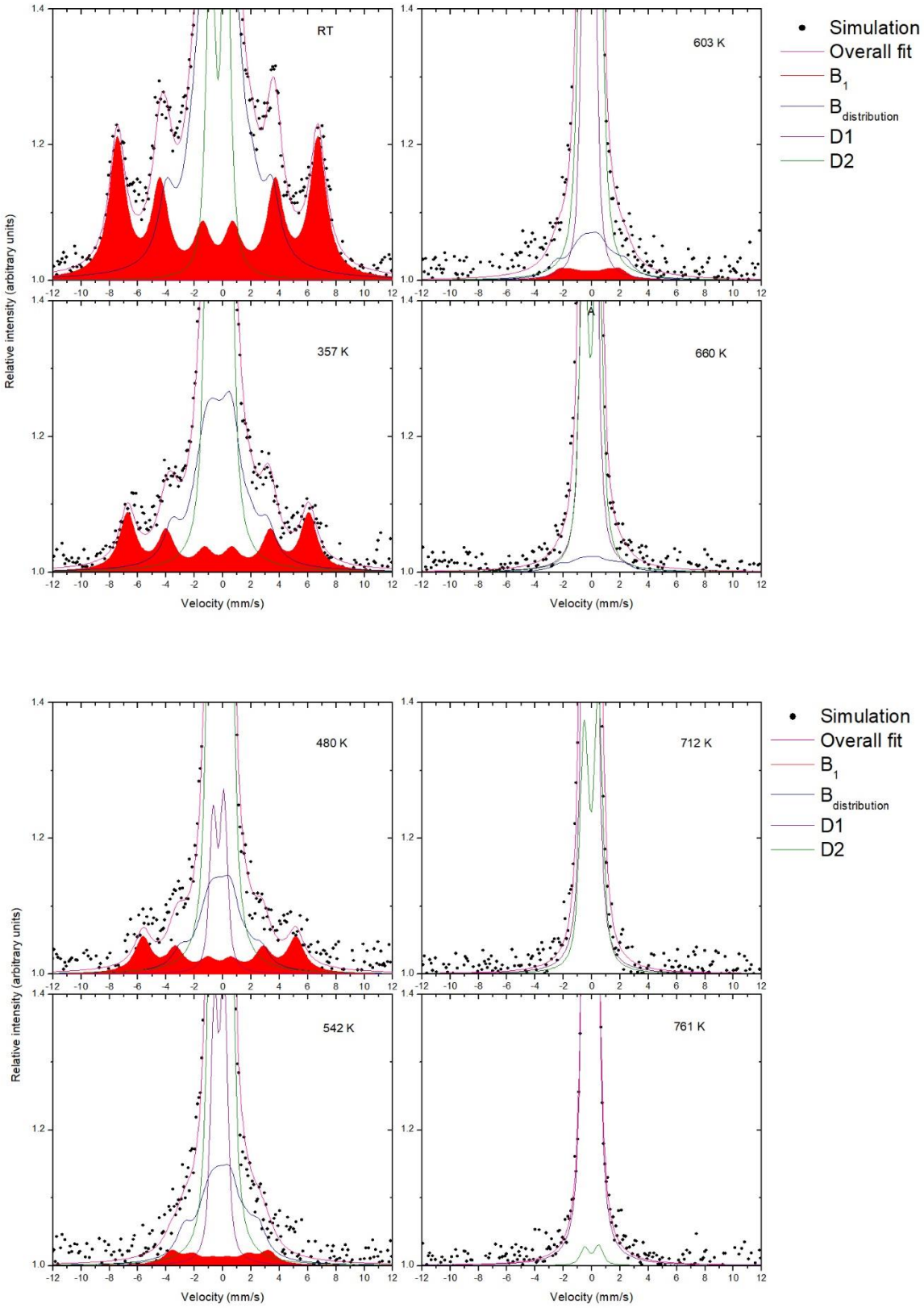

Figure 4.2: Mössbauer spectra of the BBFO *(94* nm*) sample observed at the temperatures indicated in Figure 4.1 on a smaller vertical scale.*

4.1.2 Hyperfine parameters

A summary of the fit parameters at room temperature for all spectral components is given in Table 4.1.

Table 4.1: Fit parameters obtained for BBFO *sample of 94* nm *size at room temperature, where,* $B_{distribution}$ *is a combination of two sextets.*

Spectral component	δ (mm s^{-1})	ΔE_Q ($mm\ s^{-1}$)	B_{hf}(T)	*Area* %
B_1	0.36(5)	0.00(1)	43.54(8)	30.7
$B_{distribution}$	0.27(4)	0.05(1)	22.90(3)- 7.09(6)	50.6
$D1$	0.43(1)	1.08(7)	-	0.00
$D2$	0.32(8)	1.09(1)	-	18.7

4.1.3 Annealing behavior

Figure 4.3 shows the isomer shift variation with increasing temperature for the spectral components. The isomer shifts for all spectral components follow the second order Doppler shift which is proportional to $(v/c)^2$, hence, the linear decrease with temperature [22, 26].

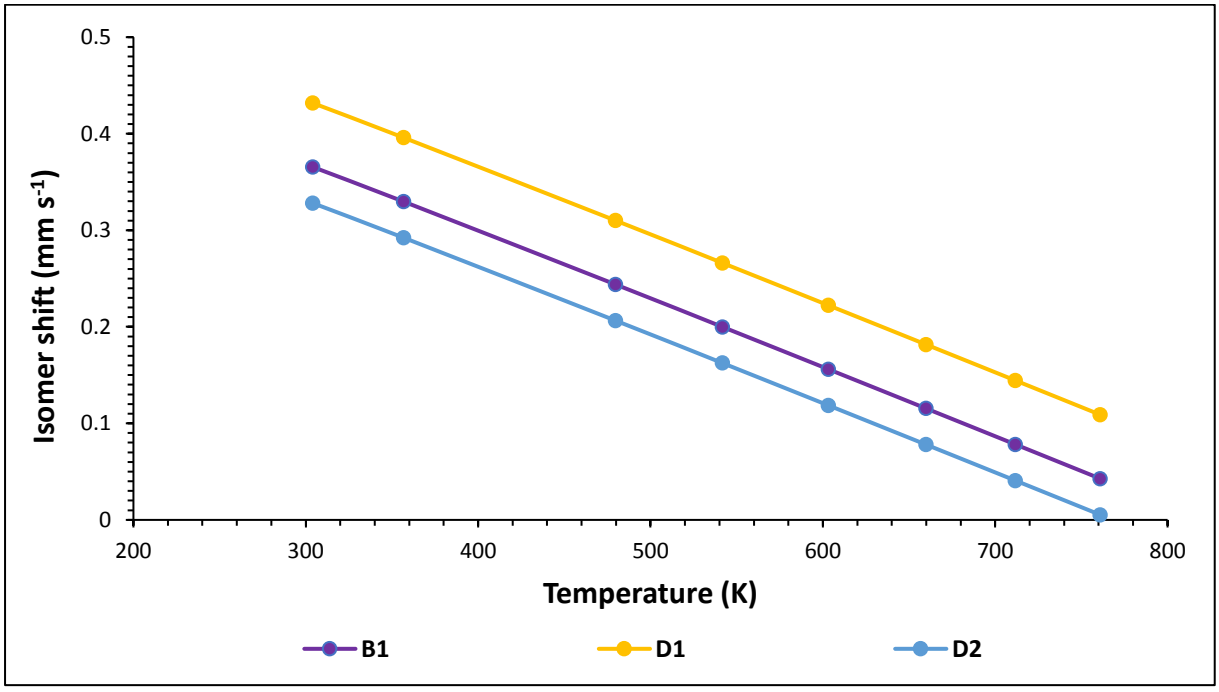

Figure 4.3: The isomer shifts as a function of temperature of the spectral components of the BBFO *sample of 94* nm *size.*

Figure 4.4 shows the quadrupole splitting, ΔE_Q variation with increasing temperature for the spectral components. The quadrupole splitting of Doublet 1 decreases quite dramatically, from $\Delta E_Q = 1.08(7)\ \mathrm{mm\ s^{-1}}$ at RT to $0.52(4)\ \mathrm{mm\ s^{-1}}$ at 761 K, as compared to Doublet 2 which remains fairly constant, with $\Delta E_Q = 1.09(1)\ \mathrm{mm\ s^{-1}}$ at RT to 0.98(4) $\mathrm{mm\ s^{-1}}$ at 761 K. The temperature dependent decrease follows a trend that would be expected with annealing [22, 26].

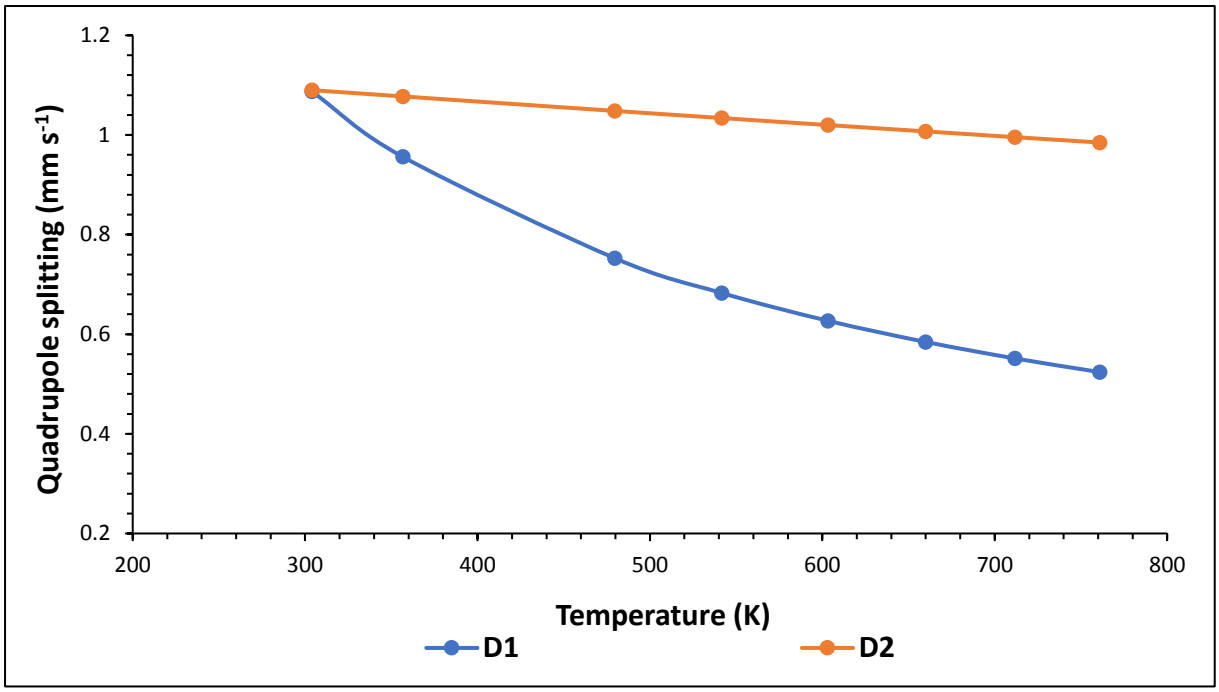

Figure 4.4: The quadrupole splitting as a function of temperature of the spectral components of the BBFO *sample of 94* nm *thickness.*

The fractional area of the of the sextet spectral component decreases rapidly with temperature, as seen in Figure 4.5. At $T > 588\ \mathrm{K}$, the total contribution of the magnetic components is less than 2% which Fischer *et al.* [35] attribute to the Curie temperature. In Fischer's neutron diffraction study of the temperature dependence of the structural and magnetic order parameters of BFO [35], they determined the Néel temperature, T_N, to be 595±10 K and that the transitions from ferroelectric to paramagnetic occur at around 600 K. For Doublet 2, this spectral component has a site population of around 18% at RT then gradually increases to its maximum contribution of around 60% at 480 K and approaches zero fractional area at the maximum temperature of 761 K. The area fraction of Double 1 increases from 0% at RT to around 99% at 761 K.

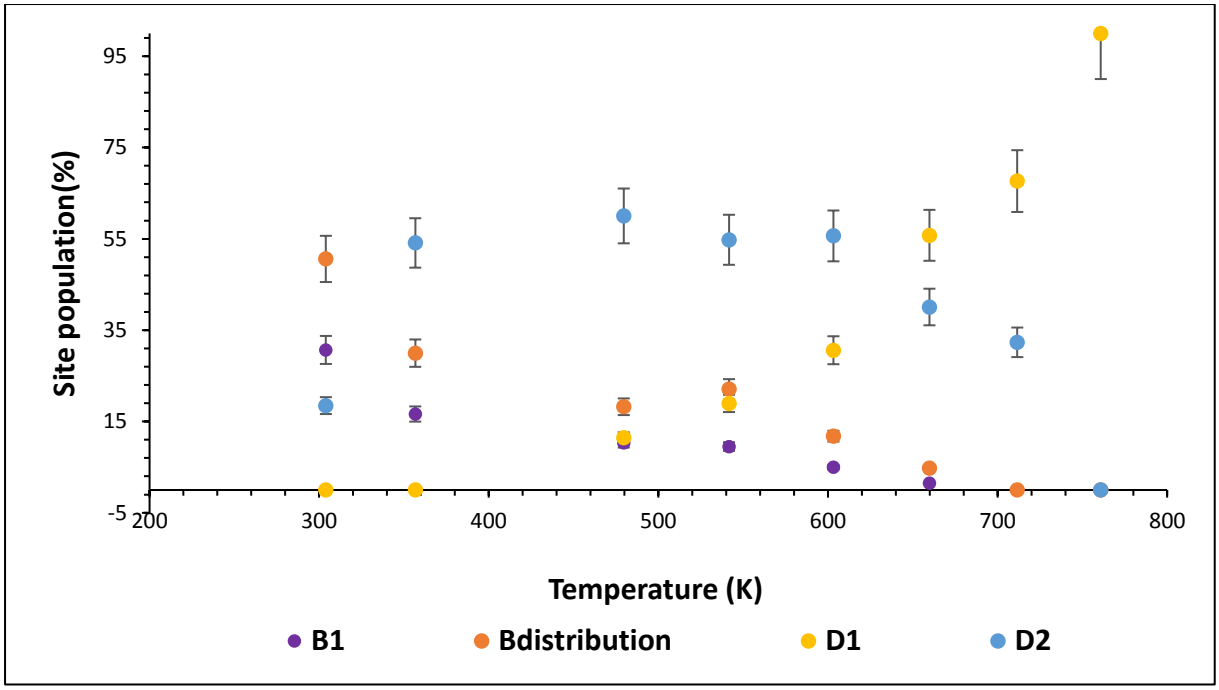

Figure 4.5: The site population dependence as a function of temperature of the spectral components of the BBFO *sample of 94* nm *thickness.*

4.2 Analysis of data and results of BBFO sample of thickness 300 nm

4.2.1 Mössbauer spectra

Figure 4.6 displays the Mössbauer spectra obtained for the Ba substituted $BiFeO_3$ (BBFO) sample of thickness 300 nm.

Similar to the 94 nm sample discussed in section 4.1, the spectra were fitted with the following spectral components: a symmetric sextet, B_1, that is modeled by a Blume-Tjon line shape, two doublets, D1 and D2, modeled by a Voigt line shape quadrupole split component, one of which is asymmetric and the other is symmetric and a magnetic distribution, $B_{distribution}$, which is a combination of two sextets that are attributed to Fe in implantation induced defects.

The room temperature (RT) spectrum is characterized by two sextets, an asymmetric doublet and a symmetric doublet as seen in Figure 4.6, whereas at higher temperatures, the spectrum is dominated by the asymmetric doublet. In Figure 4.7, the Mössbauer spectra shown in Figure 4.1 are presented here on a smaller vertical scale so that the fitting of the main magnetic component may be studied in greater detail.

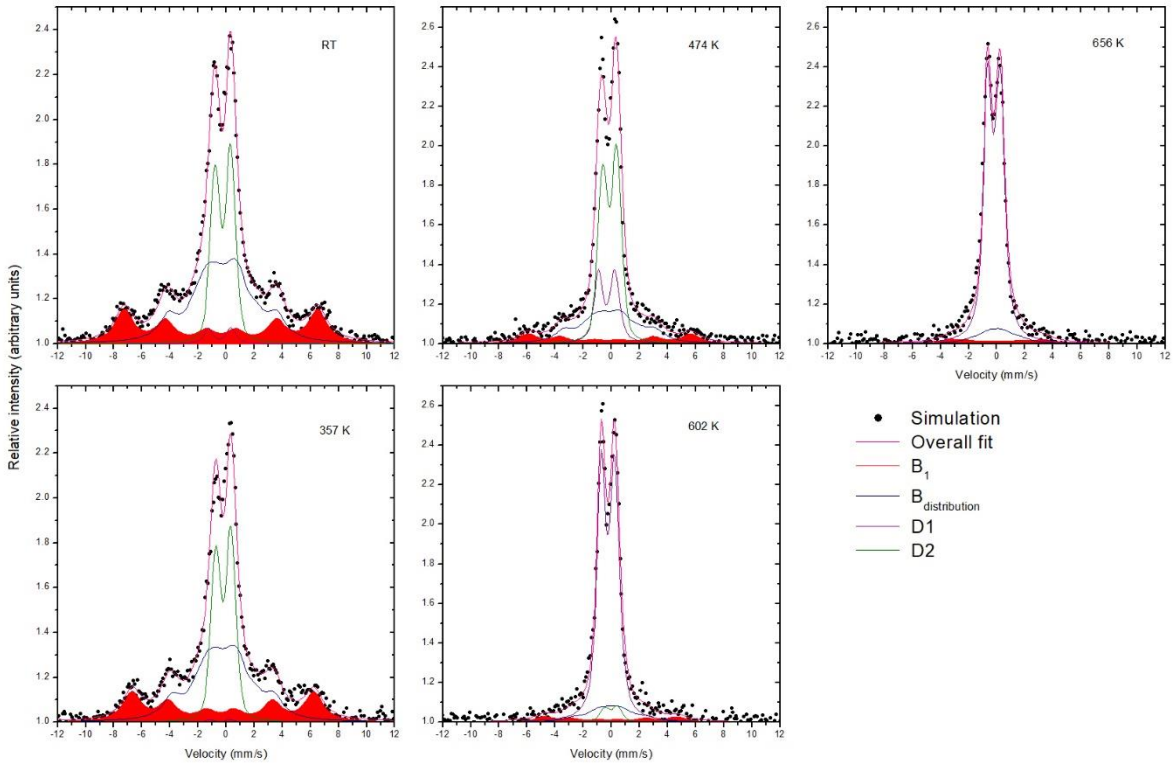

Figure 4.6: Mössbauer spectra of the BBFO *sample of 300* nm *thickness observed at the temperatures indicated.*

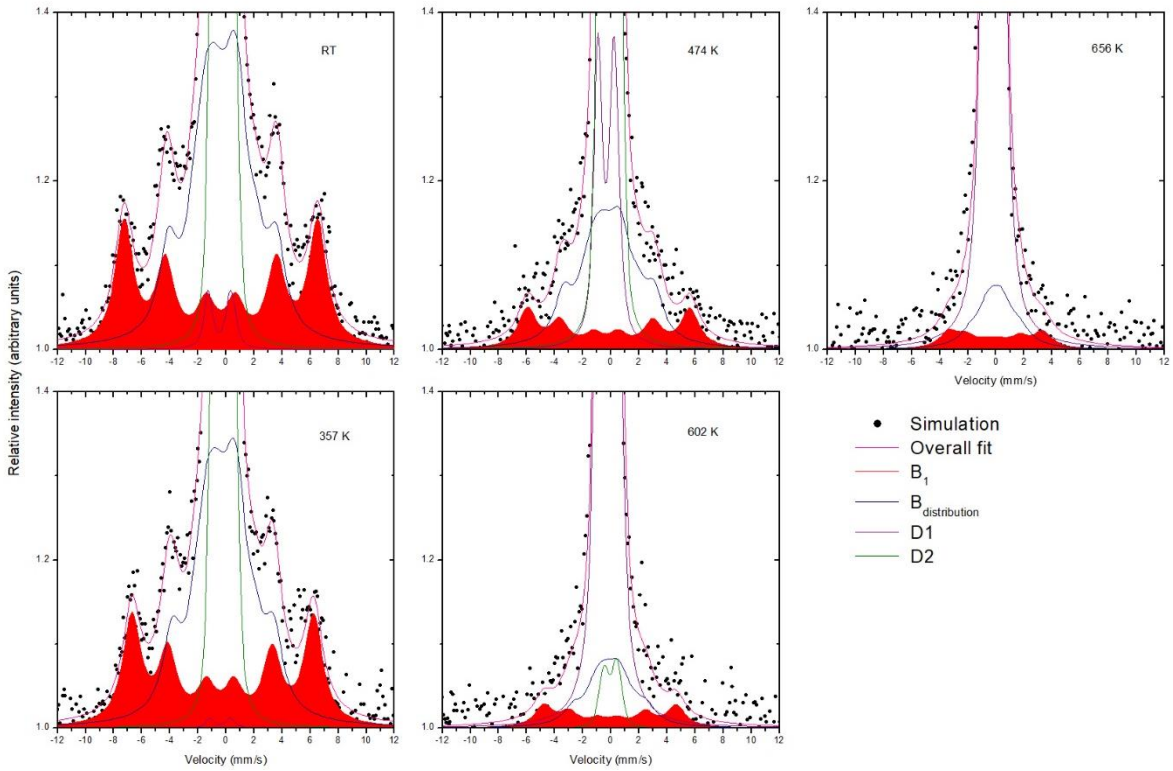

Figure 4.7: Mössbauer spectra of the BBFO *sample of 300* nm *thickness shown on a smaller vertical scale.*

4.2.2 Hyperfine parameters

A summary of the fit parameters for all spectral components is given in Table 4.2.

Table 4.2: Fit parameters obtained for BBFO *sample of 300* nm *thickness at room temperature, where,* $B_{distribution}$ *is a combination of two sextets.*

Spectral component	δ (mm s^{-1})	ΔE_Q (mm s^{-1})	B_{hf}(T)	*Area* %
B_1	0.36(5)	0.01(6)	42.33(4)	25.1
$B_{distribution}$	0.27(4)	0.05(1)	23.62(8) - 7.70(2)	43.1
$D1$	0.45(5)	1.60(4)	-	2.6
$D2$	0.23(8)	1.10(4)	-	29.2

4.2.3 Annealing behavior

Figure 4.8 shows the isomer shift variation with increasing temperature for the spectral components. The isomer shifts for all spectral components follow the second order Doppler shift, hence, the systematic decrease.

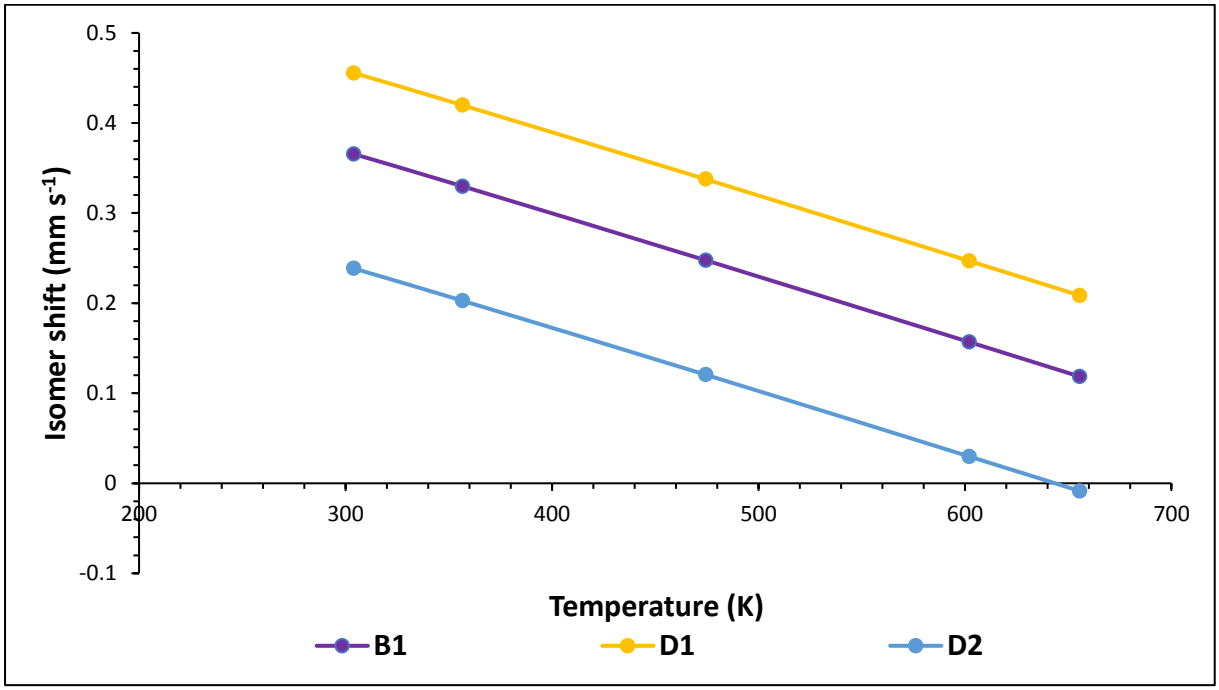

Figure 4.8: The isomer shifts as a function of temperature of the spectral components of the BBFO *sample of 300* nm *thickness.*

Figure 4.9 illustrates the quadrupole splitting variation with increasing temperature for the doublet spectral components. The ΔE_Q value of Doublet 1, $\Delta E_Q = 1.60(4)$ mm s^{-1} at RT to $\Delta E_Q = 0.88(6)$ mm s^{-1} at 656 K, decreases quite dramatically as compared to Doublet 2

which remains fairly constant, $\Delta E_Q = 1.10(4)\ \mathrm{mm\ s^{-1}}$ at RT to $\Delta E_Q = 0.88(9)\ \mathrm{mm\ s^{-1}}$ at 656 K.

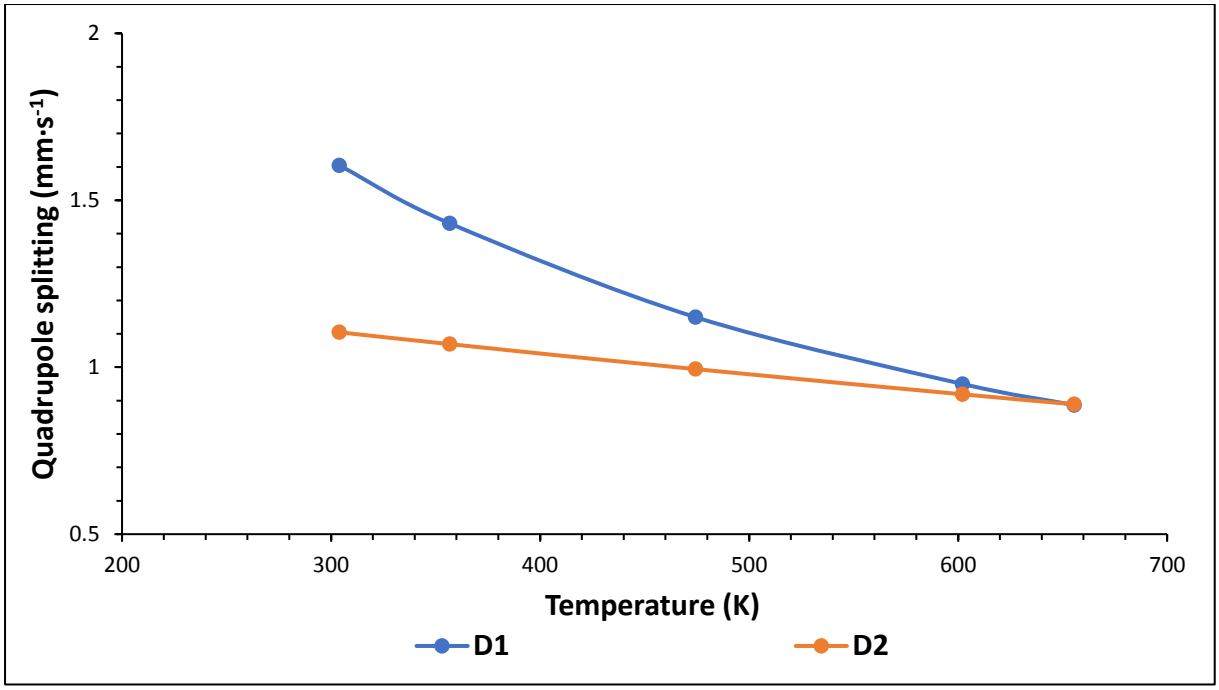

Figure 4.9: The quadrupole splitting as a function of temperature of the spectral components of the BBFO *sample of 300* nm *thickness.*

The fractional area of both of the sextet spectral components, as seen in Figure 4.10, decrease gradually where the combined contribution of the two magnetic components at 656 K is around 15%. For Doublet 2, this spectral component has a site population of around 29% at RT then gradually increases to its maximum contribution of around 45% at 474 K and approaches 3% fraction of area at maximum temperature of 656 K. The area fraction of Double 1 increases from around 1% at RT to around 84% where it dominates the spectrum at 761 K.

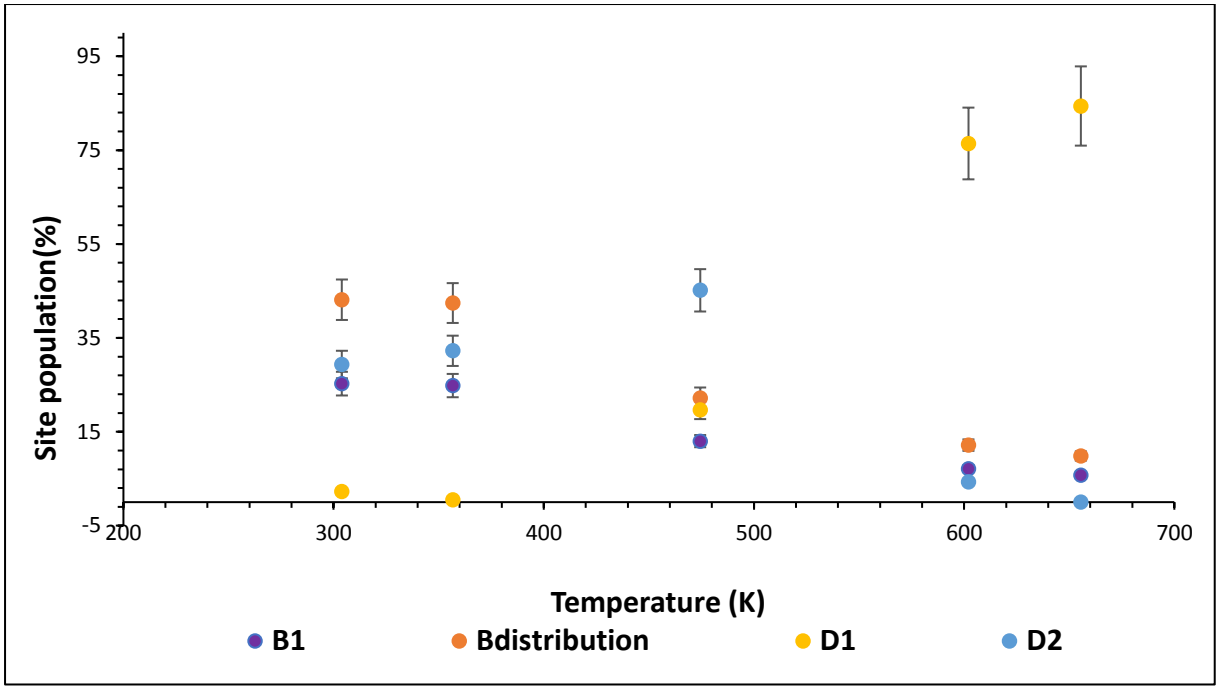

Figure 4.10: The site population dependence as a function of temperature of the spectral components of the *BBFO* sample of 300 *nm* thickness.

4.3 Analysis of data and results of the undoped BFO sample

4.3.1 Mössbauer spectra

Figure 4.11 displays the Mössbauer spectra obtained for the undoped $BiFeO_3$ (BFO) sample where figures 4.11 (c) and (d) are the same as (a) and (b), however, on a smaller vertical scale so that the main magnetic component may be studied in greater detail.

Slightly similar to the Barium doped samples discussed in sections 4.1 and 4.2, the spectra were fitted with the following spectral components: a symmetric sextet, B_1, that is modeled by a Blume-Tjon line shape, two symmetric doublets, D1 and D2, modeled by a Voigt line shape quadrupole split component and a magnetic distribution, B_2, which is a combination of two sextets that are attributed to Fe in implantation induced defects.

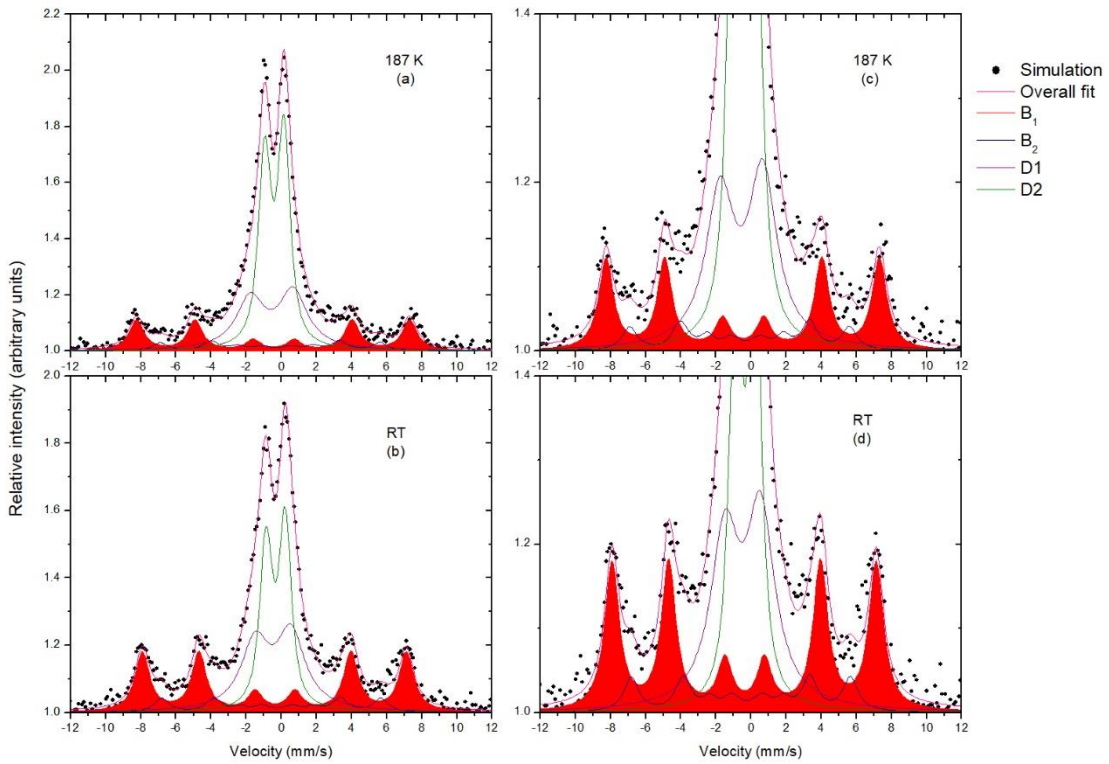

Figure 4.11: Mössbauer spectra of the undoped BFO *sample observed at the temperatures indicated where, figures (c) and (d) are on a smaller vertical scale than (a) and (b).*

4.3.2 Hyperfine parameters

A summary of the fit parameters and area fraction for all spectral components is given in Table 4.3.

Table 4.3: Fit parameters obtained for BFO *sample.*

Spectral component	δ (mm s^{-1})	ΔE_Q (mm s^{-1})	B_{hf} (T)	*Area* %
B_1	0.38(1)	0.03(4)	46.23(6)	30.4
B_2	0.27(6)	0.05(1)	22.38(1) - 38.32(5)	8.5
$D1$	0.47(4)	2.03(3)	-	30.2
$D2$	0.33(1)	1.09(6)	-	30.9

4.3.3 Annealing behavior

The quadrupole splitting ΔE_Q value of Doublet 1 decreases gradually, from $\Delta E_Q = 2.44(1)\ \mathrm{mm\ s^{-1}}$ at 187 K to $\Delta E_Q = 2.09(3)\ \mathrm{mm\ s^{-1}}$ at RT, as compared to Doublet 2 which remains fairly constant at $1.09(2)\ \mathrm{mm\ s^{-1}}$.

4.4 Temperature dependence of the magnetic field B_{hf} of the primary sextet

The samples were implanted with ^{57}Mn which via β-decay during the lifetime of the parent nucleus produces ^{57}Fe ions of 45 eV average energy. This energy allows the ^{57}Fe ions to replace ions in the sample matrix. Due to its dilute concentration, these ions prove to be suitable probes of the immediate environment. ^{57}Fe remains either in the implanted ^{57}Mn site or produces complexes as implantation defects with O_2 vacancies. Hence, the fitting of the spectra with the $B_{distribution}$ component and Doublet components, respectively.

The main focus in discussing the results obtained is the temperature dependence of the spectral component of the magnetic structure characterized by the room temperature parameters presented in Table 4.4.

Table 4.4: Hyperfine parameters obtained for all *samples.*

	B_{hf} (T)	δ (mm s^{-1})	ΔE_Q (mm s^{-1})
BBFO (94 nm)	43.54(8)	0.36(5)	0.01(1)
BBFO(300 nm)	42.33(4)	0.36(5)	0.01(6)
undoped BFO	46.23(6)	0.38(1)	0.03(4)

This component is assigned due to the anti-ferromagnetic behaviour of the BFO sample, and to ferromagnetic behaviour on the Ba doped samples. The remaining spectral components are assigned to Fe in implantation induced defects. The results of the temperature dependence of the magnetic field B_{hf} determined from the analyses of the EMS spectra of the BFO and BBFO samples as well as the fractional area are shown in Table 4.5 below.

Table 4.5: Table of B_{hf} and areal fractional as a function of temperature.

	BBFO (94 nm)		BBFO(300 nm)		undoped BFO	
T (K)	B_{hf} (T)	$Area$ %	B_{hf} (T)	$Area$ %	B_{hf} (T)	$Area$ %
187	-	-	-	-	47.83(5)	20
300	44.27(4)	27.3	43.68(4)	28.8	46.23(5)	30.2
357	39.84(4)	9.5	39.31(4)	35.9	-	-
474	-	-	35.18(4)	19.8	-	-
480	33.62(3)	13.8	-	-	-	-
542	31.13(3)	9.2	-	-	-	-
602	-	-	28.69(3)	12.2	-	-
603	29.06(3)	10.1	-	-	-	-
656	-	-	20.32(2)	17.2	-	-
660	29.1(3)	0	-	-	-	-

Figure 4.12, presents a plot of the results of the temperature dependence of the magnetic field B_{hf} determined from the analyses of the EMS spectra of the BFO and BBFO samples. In order to compare the results obtained in the present investigation with those of Kim et al. [16], the B_{hf} values had to be normalized to a saturation magnetization 48 T and the temperature to a Néel/ Curie temperature of 700 K. The results of this study are in reasonable agreement with the Brillouin curve for high spin s = 5/2 extracted from the data of Kim et al. [16].

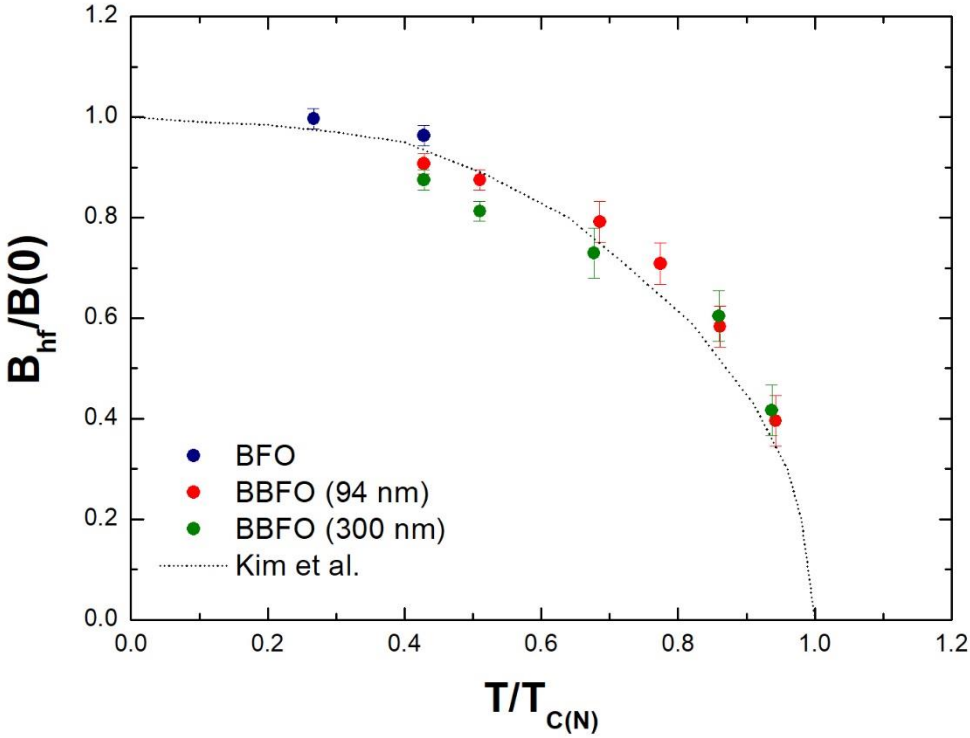

Figure 4.12: The plot of normalised B_{hf} as a function of Temperature/700 K for BFO, BBFO (94 nm and 300 nm thickness) and BBFO results of Kim et al. [16] where, the dotted curve is the magnetization curve calculated with the Brillouin function for spin s = 5/2.

5 CONCLUSIONS

Mössbauer measurements were conducted over a range of temperatures from 300 K to around 660 K on Ba doped $BiFeO_3$ and at 180 K and 300 K on undoped $BiFeO_3$. The final spectral fitting was performed simultaneously using a set of macros described in Vinda [34]. The spectra were fitted with the following spectral components - a symmetric sextet, two quadrupole split doublets modeled by Voigt line shapes and a magnetic distribution due to Fe in defect sites in the substrates. All the spectra were characterized by a decrease of B_{hf} with an increase in temperature, which is an indication of magnetic order, either ferromagnetic or antiferromagnetic. In BFO, it is antiferromagnetic where the spins are aligned anti-parallel, although, they do not cancel completely, hence, leaving a residual magnetization. Comparison of the results obtained in the present investigation with those of Kim *et al.* [16] support the conclusion that in the Ba doped BFO samples, ferromagnetic order exists, as has been reported previously.

In order to obtain a better understanding of the ferroelectric and magnetic properties of these materials, complementary measurements are needed such as magnetization measurements using a Superconducting Quantum Interference Device (SQUID), Electron Paramagnetic Resonance (EPR) and Nuclear Magnetic Resonance (NMR) measurements.

Within the Mössbauer Collaboration studies were carried out on other oxide materials that have demonstrated the presence of magnetic features showing slow spin-lattice relaxation [46-48]. In these studies, the signature for the spin-lattice relaxation was that the magnetic field remained constant in value while the linewidth increased with temperature due to the spin-lattice relaxation process. However, in the present study, as seen in Figure 4.12, the magnetic field decreases rapidly with an increase in temperature illustrating that we are observing ferromagnetic behavior. However, a difficulty encountered in the analyses was the fact that together with the decrease in magnetic field strength there was a marked decrease of the intensity of the Fe^{3+} component with increasing temperature. The isomer shift remained characteristic of Fe^{3+}. From this we concluded that, more contribution from Fe^{3+} ions was found in the central doublet and not in the main magnetic component. This feature

is not unexpected if the magnetic structure that was observed is due to defects which then anneal at higher temperatures, therefore, the decrease in intensity of the magnetic component.

REFERENCES

[1] N. A. Spaldin and M. Fiebig, “The Renaissance of Magnetoelectric Multiferroics,” *SCIENCE,* vol. 309, pp. 391-392, 15 July 2005.

[2] G. Yahia, F. Damay, S. Chattopadhyay, V. Balédent, W. Peng, E. Elkaim, M. Whitaker, M. Greenblatt, M.-B. Lepetit and P. Foury-Leylekian, “Recognition of exchange striction as the origin of magnetoelectric coupling in multiferroics,” *Phys. Rev.,* vol. 95, no. 18, 2017.

[3] V. V. Lazenka, G. Zhang, J. Vanacken, I. I. Makoed, A. F. Ravinski and V. V. Moshchalkov, “Structural transformation and magnetoelectric behaviour in Bi1−xGdxFeO3 multiferroics,” *Journal of Physics D: Applied Physics,* vol. 45, 2012.

[4] M. El–Desoky, M. Ayoua, M. Mostafa and M. Ahmed, “Multiferroic properties of nanostructured barium doped bismuth ferrite,” *Journal of Magnetism and Magnetic Materials,* vol. 404, pp. 68-73, 2016.

[5] R. Haumont, I. A. Kornev, S. Lisenkov, L. Bellaiche, J. Kreisel and B. Dkhil, “Phase stability and structural temperature dependence in powdered multiferroic BiFeO3,” *PHYSICAL REVIEW B,* vol. 78, 2008.

[6] D. H. Wang, W. C. Goh, M. Ning and C. K. Ong, “Effect of Ba doping on magnetic, ferroelectric, and magnetoelectric properties in mutiferroic BiFeO3 at room temperature,” *Applied Physics Letters,* vol. 88, 2006.

[7] V. Naik and R. Mahendiran, “Magnetic and magnetoelectric studies in pure and cation doped BiFeO3,” *Solid State Communications,* vol. 149, pp. 754-758, 2009.

[8] V. R. Palkar, D. C. Kundaliya and S. K. Malik, “Effect of Mn substitution on magnetoelectric properties of bismuth ferrite system,” *Journal of Applied Physics,* vol. 93, pp. 4337-4339, 2003.

[9] P.Fischer, M.Polomska, I.Sosnowska and M.Szymanski, “Temperature dependence of the crystal and magnetic structures of BiFeO3,” *Journal of Physics C: Solid State Physics,* vol. 13, 1980.

[10] J. T. Zhang, X. M. Lu, J. Zhou, H. Sun, J. Su, C. C. Ju, F. Z. Huang and J. S. Zhu, “Origin of magnetic anisotropy and spiral spin order in multiferroic BiFeO3,” *Appl. Phys. Lett.,* vol. 100, p. 242413, 2012.

[11] J. Gebhardt and A. M. Rappe, “Doping of BiFeO3: A comprehensive study on substitutional doping,” *PHYSICAL REVIEW B,* vol. 98, p. 125202, 2018.

[12] A. I. Klyndyuk and E. A. Chizhova, “Structure, Thermal Expansion, and Electrical Properties of BiFeO3–NdMnO3 Solid Solutions,” *Inorganic Materials,* vol. 51, pp. 272-277, 2015.

[13] J. Liu, F. Gao, G. L. Yuan, Y. Wang, M. Zeng and J. G. Wan, “Ferroelectric and magnetoelectric behaviors of multiferroic BiFeO3 and piezoelectric-magnetostrictive composites,” *J Electroceram,* vol. 21, pp. 78-84, 2008.

[14] C. Lan, Y. Jiang and S. Yang, “Magnetic properties of La and (La, Zr) doped BiFeO3 ceramics,” *Journal of Materials Science,* vol. 46, pp. 734-738, 2011.

[15] R. Das and K. Mandal, “Magnetic, ferroelectric and magnetoelectric properties of Ba-doped BiFeO3,” *Journal of Magnetism and Magnetic Materials,* vol. 324, pp. 1913-1918, 2012.

[16] W. Kim and C. S. Kim, “M¨ossbauer Study of a Polycrystalline Multiferroic Ba-doped BiFeO3 Compound,” *Journal of the Korean Physical Society,* vol. 56, no. 2, pp. 607-610, 2010.

[17] M. Li, M. Ning, Y. Ma, Q. Wu and C. K. Ong, “Room temperature ferroelectric, ferromagnetic and magnetoelectric properties of Ba-doped BiFeO3 thin films,” *JOURNAL OF PHYSICS D: APPLIED PHYSICS ,* vol. 40, pp. 1603-1607, 2007.

[18] L. Luo, W. Luo, G. Yuan, W. Wei, X. Yuan, H. Zhang, K. Shen, M. Xu and Q. Xu, “The Origin of Enhanced Room Temperature Ferromagnetism in Ba Doped BiFeO3,” *J Supercond Nov Magn,* vol. 26, pp. 3309-3313, 2013.

[19] V. Srinivas, A. T. Raghavender and K. V. Kumar, “Effect of Ba Substitution on the Structural and Magnetic Properties of BiFeO3,” *World Journal of Nano Science and Engineering,* vol. 6, pp. 38-44, 2016.

[20] R. Mössbauer, “The discovery of the Mössbauer effect,” *Hyperfine Interactions,* vol. 126, pp. 1-12, 2000.

[21] S. S. Hanna, “The early iron age of the Mössbauer era,” *Hyperfine interactions,* vol. 90, pp. 3-20, 1994.

[22] N. Greenwood and T. Gibb, Mössbauer Spectroscopy, London: Chapman and Hall Ltd, 1971.

[23] G. Long and F. Grandjean, “2.20 - Mössbauer Spectroscopy: Introduction,” in *Comprehensive Coordination Chemistry II*, Elsevier, 2003, pp. 269-277.

[24] H. Masenda, “Are Fe and Co implanted ZnO and III-nitride semiconductors magnetic?,” PhD thesis, University of the Witwatersrand, Johannesburg, 2014.

[25] W. B. Dlamini, “^{57}Fe Mössbauer studies of 57Mn* implanted III-V semiconductors InP and InAs,” MSC dissertation, University of KwaZulu-Natal, Durban, 2011.

[26] M. Ncube, “An investigation of the structural and magnetic properties of Ho substituted BiFeO3,” MSc dissertation, University of the Witwatersrand, Johannesburg, 2012.

[27] D. Naidoo, “57Fe MÖSSBAUER INVESTIGATIONS IN DIAMOND, SiGe AND Ge SINGLE CRYSTALS,” PhD thesis, University of KwaZulu-Natal, Durban, 2006.

[28] T. E. Mølholt, “Paramagnetism in ion-implanted oxides,” PhD thesis, University of Iceland, Reykjavík, 2012.

[29] P. Gütlich, B. Eckhard and A. X. Trautwein, Mössbauer Spectroscopy and Transition Metal Chemistry, Heidelberg: Springer , 2011.

[30] G. Koster, B. L. Kropman, G. J. H. M. Rijnders, D. H. A. Blank and H. Rogalla, “Quasi-ideal strontium titanate crystal surfaces through formation of strontium hydroxide,” *Applied Physics Letters,* vol. 73, p. 2920, 1998.

[31] C. Mix and G. Jakob, “Multiferroic and structural properties of BiFeO3 close to the strain induced phase transition on different substrates,” *Journal of Applied Physics,* vol. 113, p. 17D907, 2013.

[32] J. G. Stevens and R. S. Preston, Mössbauer effect data index, New York: IFI/ Plenum, 1972.

[33] J. F. Ziegler, J. P. Biersack and M. D. Ziegler, The Stopping and Range of Ions in Matter, 2015.

[34] H. P. Gunnlaugsson, “Vinda:users-phys.au.dk/hpg/vinda.htm.,” 2011.

[35] P. Fischer, M. Polomska, I. Sosnowska and M. Szymanski, *J. Phys. C: Solid State Phys.,* vol. 13, pp. 1931-1940, 1980.

[36] P. Atkins and J. De Paula, Physical Chemistry, Oxford: Oxford University Press, 2006.

[37] E. Kuzmann, S. Nagy and A. Vertes, “Critical review of analytical applications of Mössbauer spectroscopy illustrated by mineralogical and geological examples,” *Pure Appl. Chem.,* vol. 75, pp. 801-858, 2003.

[38] H. J. Lipkin, *Ann. Phys.,* vol. 9, p. 332, 1960.

[39] H. Frauenfelder, The Mossbauer Effect, New York: W. A. Benjamin, Inc., 1962.

[40] V. Weisskopf and E. Wigner, *Z. Physik,* vol. 63, p. 54, 1930.

[41] V. Weisskopf and E. Wigner, *Z. Physik,* vol. 65, p. 18, 1930.

[42] G. Pake, Paramagnetic Resonance, New York: W. A. Benjamin, 1962.

[43] A. Abragam and B. Bleaney, Electron Paramagnetic Resonance of Transition Ions, Oxford: Clarendon, 1970.

[44] R. Herber, “Structure, bonding and the Mössbauer lattice temperature,” in *Chemical Mössbauer Spectroscopy*, New York, Plenum, 1984.

[45] G. Shenoy and B. Dunlop, *Nucl. Instrum. Methods,* vol. 71, p. 285, 1969.

[46] J. T. Zhang, X. M. Lu, J. Zhou, H. Sun, J. Su, C. C. Ju, F. Z. Huang and J. S. Zhu, “Origin of magnetic anisotropy and spiral spin order in multiferroic BiFeO3,” *Appl. Phys. Lett.,* vol. 100, p. 242413, 2012.

[47] T. E. Mølholt et al., “Spin–lattice relaxations of paramagnetic Fe3+ in ZnO,” *Phys. Scr.,* p. 014006, 2012.

[48] T. E. Mølholt et al., *Hyperfine Interact.,* vol. 197, p. 89, 2010.

[49] H. P. Gunnlaugsson et al., *Hyperfine Interact.,* vol. 198, p. 5, 2010.